British Geological Survey

Geomechanical and Acoustic Characterisation of Gassum Formation Sandstones from Stenlille, Denmark

Multi-Hazards and Resilience Programme

Open report OR/26/072

BRITISH GEOLOGICAL SURVEY

MULTI-HAZARDS AND RESILIENCE PROGRAMME

OPEN REPORT OR/26/072

The National Grid and other Ordnance Survey data © Crown Copyright and database rights 2025. OS AC0000824781.

Keywords

Geomechanics, Gassum Formation, drained triaxial testing, rock strength, elastic properties, acoustic velocity.

Bibliographical reference

RD Valdez II, J Chen, A Ougier-Simonin, N Andrianov, & SJ Oldfield, 2026. Geomechanical and Acoustic Characterisation of Gassum Formation Sandstones from Stenlille, Denmark. *British Geological Survey Open Report*, OR/26/072. 40pp.

Copyright in materials derived from the British Geological Survey's work is owned by UK Research and Innovation (UKRI) and/or the authority that commissioned the work. You may not copy or adapt this publication without first obtaining permission. Contact the BGS Intellectual Property Rights Section, British Geological Survey, Keyworth, email ipr@bgs.ac.uk. You may quote extracts of a reasonable length without prior permission, provided a full acknowledgement is given of the source of the extract.

Geomechanical and Acoustic Characterisation of Gassum Formation Sandstones from Stenlille, Denmark

RD Valdez II, J Chen, A Ougier-Simonin, N Andrianov, SJ Oldfield

© UKRI 2026. All rights reserved

Keyworth, Nottingham British Geological Survey 2026

BRITISH GEOLOGICAL SURVEY

The full range of our publications is available from the BGS online shop at https://shop.bgs.ac.uk/ and our Cardiff office (Welsh publications only). The London Information Office also maintains a reference collection of BGS publications, including fossils, for consultation. We publish an annual catalogue of our maps and other publications; this catalogue is also available online.

The British Geological Survey carries out the geological survey of Great Britain and Northern Ireland (the latter as an agency service for the government of Northern Ireland), and of the surrounding continental shelf, as well as basic research projects. It also undertakes programmes of technical aid in geology in developing countries.

The British Geological Survey is a component body of UK Research and Innovation.

British Geological Survey offices

Nicker Hill, Keyworth,
Nottingham NG12 5GG
Tel 0115 936 3100

BGS Central Enquiries Desk
Tel 0115 936 3143
email enquiries@bgs.ac.uk

BGS Sales
Tel 0115 936 3241
email sales@bgs.ac.uk

The Lyell Centre, Research Avenue South,
Edinburgh EH14 4AP
Tel 0131 667 1000
email scotsales@bgs.ac.uk

Natural History Museum, Cromwell Road,
London SW7 5BD
Tel 020 7589 4090
Tel 020 7942 5344/45
email bgslondonstaff@bgs.ac.uk

Cardiff University, Main Building, Park Place,
Cardiff CF10 3AT
Tel 029 2167 4280

Geological Survey of Northern Ireland, 7th Floor,
Adelaide House, 39-49 Adelaide Street, Belfast, BT2 8FD
Tel 0289 038 8462
www2.bgs.ac.uk/gsni/

Natural Environment Research Council, Polaris House,
North Star Avenue, Swindon SN2 1EU
Tel 01793 411500 Fax 01793 411501
www.nerc.ac.uk

UK Research and Innovation, Polaris House,
Swindon SN2 1FL
Tel 01793 444000
www.ukri.org

Website: https://www.bgs.ac.uk
Shop online: https://shop.bgs.ac.uk/

Foreword

This report presents the results of a laboratory study conducted by the British Geological Survey (BGS) to characterise the geomechanical and acoustic properties of Gassum Formation sandstone from the Stenlille site, Denmark. The testing was conducted in the Rock Mechanics and Physics Laboratory at BGS, Keyworth, UK, using a servo-controlled triaxial rock testing system. The experimental programme consisted of 15 drained triaxial compression tests on five sandstone types from the Stenlille-5, Stenlille-6, Stenlille-13 and Stenlille-14 wells. The testing provided measurements of strength, static and dynamic elastic properties, and acoustic velocities, together with Mohr-Coulomb failure parameters for the tested sandstone types.

Acknowledgements

This study was undertaken by staff from the British Geological Survey (BGS) in collaboration with the Geological Survey of Denmark and Greenland (GEUS), with laboratory testing also undertaken by Jinci Chen, a joint BGS and Heriot-Watt University PhD student. GEUS/Gas Storage Denmark provided the Stenlille core material and supporting geological and well information used in the study.

This work was completed as part of the ConsenCUS project (Carbon Neutral Clusters through Electricity-based Innovations in Capture, Utilisation and Storage), led at BGS by Audrey Ougier-Simonin. The ConsenCUS project received funding from the European Union's Horizon 2020 Research and Innovation Programme under grant agreement No. 101022484. Additional information on the ConsenCUS project is available from the ConsenCUS project website (https://consencus.eu) or by contacting info@consencus.eu. All other enquiries should be directed to the corresponding author.

All laboratory testing was conducted in the Rock Mechanics and Physics Laboratory at BGS, Keyworth, UK, with Jinci Chen conducting the majority of the tests and BGS staff undertaking the remaining testing. Subsequent data analysis and interpretation were undertaken at BGS. Nikolai Andrianov led the GEUS contribution to the study, working with Simon Oldfield to provide the supporting geological and well information required for the experimental programme. Simon Oldfield also carried out the well log analysis and overburden calculations used to estimate the vertical stress conditions at Stenlille.

Contents

Foreword ii

Acknowledgements ii

Contents iii

Summary vi

1 Introduction 1

2 Sample Preparation & Experimental Setup 1

3 Experimental Programme & Procedure 3
- 3.1 Sample Selection, Test Conditions, & Pore Fluid Chemistry 3
- 3.2 Experimental Procedure 4

4 Mechanical Property & Failure Analysis 5
- 4.1 Stress, Strain, & Peak Strength 5
- 4.2 Static Elastic Parameters 6
- 4.3 Mohr-Coulomb Failure Analysis 6
- 4.4 Acoustic Velocities & Dynamic Elastic Parameters 7

5 Results 8
- 5.1 Mechanical Results 8
- 5.2 Acoustic Velocity & Dynamic Elastic Results 18

6 Concluding Remarks 20

Appendix 1 Synthetic Brine Composition 21

Appendix 2 Estimation of Overburden Stress 22

Appendix 3 Acoustic Velocity & Dynamic Elastic Data 25

Glossary 29

References 30

FIGURES

Figure 1. Triaxial setup for the MTS 815 rock test system at the British Geological Survey. 2

Figure 2. Effective axial stress and axial strain response of the three Sandstone Type 1 samples. 10

Figure 3. Relationship between peak effective axial stress and effective confining pressure for Sandstone Type 1. The dashed line shows the linear fit to the three test results, with extrapolation to zero effective confining pressure used to estimate UCS. 10

Figure 4. Mohr-Coulomb failure analysis for Sandstone Type 1. Mohr circles are shown for the three drained triaxial tests, together with the fitted failure envelope and extrapolated UCS circle. 11

Figure 5. Effective axial stress and axial strain response of the three Sandstone Type 2 samples. 11

Figure 6. Relationship between peak effective axial stress and effective confining pressure for Sandstone Type 2. The dashed line shows the linear fit to the three test results, with extrapolation to zero effective confining pressure used to estimate UCS. 12

Figure 7. Mohr-Coulomb failure analysis for Sandstone Type 2. Mohr circles are shown for the three drained triaxial tests, together with the fitted failure envelope and extrapolated UCS circle. 12

Figure 8. Effective axial stress and axial strain response of the three Sandstone Type 3 samples. 13

Figure 9. Relationship between peak effective axial stress and effective confining pressure for Sandstone Type 3. The black dashed line shows the linear fit to Plugs 32 and 33 used to determine the reported Mohr-Coulomb parameters. The grey dashed line shows the linear fit to all three test results, which produces a negative intercept at zero effective confining pressure. 14

Figure 10. Mohr-Coulomb failure analysis for Sandstone Type 3. Mohr circles are shown for the tests conducted on Plugs 32 and 33, together with the fitted failure envelope and extrapolated UCS circle. 14

Figure 11. Effective axial stress and axial strain response of the three Sandstone Type 4 samples. 15

Figure 12. Relationship between peak effective axial stress and effective confining pressure for Sandstone Type 4. The dashed line shows the linear fit to the three test results, with extrapolation to zero effective confining pressure used to estimate UCS. 15

Figure 13. Mohr-Coulomb failure analysis for Sandstone Type 4. Mohr circles are shown for the three drained triaxial tests, together with the fitted failure envelope and extrapolated UCS circle. 16

Figure 14. Effective axial stress and axial strain response of the three Sandstone Type 5 samples. 16

Figure 15. Relationship between peak effective axial stress and effective confining pressure for Sandstone Type 5. The dashed line shows the linear fit to the three test results, with extrapolation to zero effective confining pressure used to estimate UCS. 17

Figure 16. Mohr-Coulomb failure analysis for Sandstone Type 5. Mohr circles are shown for the three drained triaxial tests, together with the fitted failure envelope and extrapolated UCS circle. 17

Figure A 1. Well log data and composite density profile used to estimate vertical stress for the Stenlille-6 well. Available bulk-density and sonic-log data provided by GEUS/Gas Storage Denmark were combined with estimated densities to construct the density profile used for integration with depth. 23

Figure A 2. Well log data and composite density profile used to estimate vertical stress for the Stenlille-10 well. Available bulk-density and sonic-log data provided by GEUS/Gas Storage Denmark were combined with estimated densities to construct the density profile used for integration with depth. 24

TABLES

Table 1 Sample information for the sandstone material used in the triaxial testing programme. 3

Table 2 Test conditions for each drained triaxial compressive strength test. Depth-vertical stress profiles were derived from well log data was provided by GEUS. The logging depth of each sample was matched to this profile to estimate the corresponding in situ vertical stress. For each sandstone type, one of the three tests was conducted at a confining pressure representative of this estimated in situ vertical stress. The remaining two tests from each triplicate set were conducted at lower confining pressures to constrain the Mohr-Coulomb failure envelope. 4

Table 3 Summary of the Stenlille drained triaxial test results. Mohr-Coulomb failure parameters are shown for each sandstone type. The parameters for Sandstone Type 3 are based on Plugs 32 and 33 only and should be used with caution. 9

Table 4 Summary of the Mohr-Coulomb failure parameters for each sandstone type. Note that the parameters for Sandstone Type 3 are based on Plugs 32 and 33 only and should be used with caution. 9

Table 5. Summary of measured P-wave and orthogonally polarised S-wave velocities for the five sandstone types. Values represent the minimum and maximum recorded during differential loading. 19

Table 6. Summary of calculated isotropic-equivalent dynamic elastic properties for the five sandstone types. Values represent the minimum and maximum calculated during differential loading using P-wave velocity, S1 velocity, and bulk density. 19

Table A 1. Composition of the synthetic brine used for sample saturation and drained triaxial testing. 21

Table A 2. Calculated bulk properties of the synthetic brine. 21

Table A 3. P-wave and orthogonally polarised S-wave velocities measured at individual differential stress stages for the five selected sandstone plugs. 25

Table A 4. Calculated isotropic-equivalent dynamic elastic properties and shear-wave velocity contrast at individual differential stress stages for the five selected sandstone plugs. 27

Summary

An initial assessment of the risks to subsurface injection, storage and containment of CO_2 at the Stenlille site (ConsenCUS Deliverable D4.5), identified geomechanical instability as a potential risk. Specifically, injection-induced pressure increase may alter the in-situ stress regime and reactivate faults, creating a potential migration pathway through the caprock. Quantifying these risks requires a geomechanical model of the subsurface, which must in turn be calibrated against laboratory rock mechanics data. The Gassum Formation is also the target storage formation at several other potential CO_2 storage sites in Denmark, so data on its mechanical properties are relevant beyond Stenlille. To provide such data, the Geological Survey of Denmark and Greenland (GEUS) and the British Geological Survey (BGS), both partners in the ConsenCUS project, carried out a laboratory geomechanical testing programme on Gassum Formation sandstone from the Stenlille site.

This report presents the results of a laboratory geomechanical testing programme undertaken by the British Geological Survey on sandstone material collected from the Stenlille site, Denmark. The programme comprised 15 drained triaxial compressive strength tests on cylindrical sandstone plugs representing five sandstone types. Three plugs were tested for each sandstone type at different confining pressures to provide independent failure measurements from which a Mohr-Coulomb failure envelope could be defined and the unconfined compressive strength (UCS), cohesion, angle of internal friction and coefficient of friction estimated. Samples were selected from comparable logging depths within the same well where sufficient material was available. For Sandstone Type 5, insufficient suitable material was available from a single well and the three-test set therefore incorporated material of the same assigned lithology from Stenlille-5 and Stenlille-6.

The confining and pore pressure test conditions were selected to reflect the estimated in-situ conditions at the corresponding sample depths. GEUS provided vertical stress estimates derived from density log data, which were matched to the logging depths of the individual plugs. For each sandstone group, one test was conducted at a confining pressure approximately equivalent to the estimated in-situ vertical stress over the corresponding sample depth range, with two additional tests conducted at lower confining pressures to constrain the Mohr-Coulomb failure envelope. Confining pressures of 24 to 36 MPa were applied during testing and, with the pore pressure maintained at 16 MPa, corresponded to effective confining pressures of 8 to 20 MPa. A synthetic brine was used to replicate the in-situ pore-fluid chemistry and minimise potential rock-fluid interactions that could arise from using a generic laboratory fluid.

Axial and radial strains were continuously measured during loading and used to determine the static elastic response of the samples, including Young's modulus and Poisson's ratio. Peak effective axial stress was determined for each test, and the Mohr-Coulomb failure criterion was applied to the results from each sandstone group to estimate UCS, cohesion, angle of internal friction and coefficient of friction. Piezoelectric transducers incorporated within the end platens were additionally used to measure compressional (P-wave) and two orthogonally polarised shear-wave velocities (S1 and S2) at selected stages throughout testing. The resulting acoustic velocities and dynamic elastic properties are presented alongside the mechanical test results in this report.

Peak effective axial stress across the 15 tests ranged from 58.48 to 145.07 MPa and static Young's modulus ranged from 10.55 to 18.16 GPa. Sandstone Type 1, represented by plugs from Stenlille-5 at 1580.79–1581.10 m MD, produced the highest estimated UCS of 60.27 MPa, with a cohesion of 17.07 MPa, angle of internal friction of 30.93°, and coefficient of friction of 0.599. Sandstone Type 2 (Stenlille-14; 1684.52–1685.47 m MD) gave an estimated UCS of 43.72 MPa, cohesion of 12.82 MPa, angle of internal friction of 29.21°, and coefficient of friction of 0.559. Sandstone Type 4 (Stenlille-13; 1717.40–1719.87 m MD) gave corresponding values of 43.46 MPa, 15.17 MPa, 20.37°, and 0.371, respectively. Sandstone Type 5, represented by plugs from Stenlille-5 at 1570.95–1571.20 m MD and Stenlille-6 at 1574.50 m MD, gave an estimated UCS of 42.90 MPa, cohesion of 10.45 MPa, angle of internal friction of 38.02°, and coefficient of friction of 0.781.

The results for Sandstone Type 3 (Stenlille-6; 1581.88-1584.63 m MD) differed from the systematic strength response observed for the other sandstone groups. Peak effective axial stresses of 72.19, 97.57, and 145.07 MPa were measured across the three tests, which did not define a consistent linear relationship with effective confining pressure. A linear fit to all three peak stress values did not provide a physically meaningful estimate of UCS. The reported parameters are therefore based on Plugs 32 and 33, which were the only two-point combination that produced a positive UCS intercept. These parameters should be treated with caution because the available data are insufficient to determine the source of the variability between the three tests. Nonetheless, the resulting estimated UCS was 21.41 MPa, with a cohesion of 4.75 MPa, angle of internal friction of 42.14° and coefficient of friction of 0.904.

Acoustic measurements were analysed for one representative plug from each sandstone type to characterise P-wave and orthogonally polarised S-wave velocities and calculate isotropic-equivalent dynamic elastic properties. P-wave velocities ranged from 3219 to 3867 m/s, while dynamic Young's modulus ranged from 6.14 to 24.78 GPa. Some samples showed modest overall increases in velocity during loading, although substantial fluctuations, particularly in the shear-wave measurements for Sandstone Types 2 and 3, limited the identification of consistent stress-dependent relationships. Although acoustic measurements were generally taken up to or near peak failure, no consistent pre-failure velocity reduction was identified. Unusually low shear-wave velocities for Sandstone Types 2 and 3 also produced calculated dynamic Young's moduli below the corresponding static values at certain loading stages, suggesting potential uncertainty in some shear-wave arrival identifications. Consequently, the results provide additional characterisation of the tested sandstones but are more suitable for informing material-property ranges than for establishing reliable stress-dependent relationships.

1 Introduction

The Stenlille site is an underground natural gas storage facility, located approximately 70 km south-west of Copenhagen (Denmark). Natural gas is being stored in the upper Triassic Gassum Sandstone Formation 1500–1600 m below the surface; the subsurface has been characterized extensively (Holmslykke et al., 2020; Kristensen, 2021; Bredesen, 2022). However, no rock mechanical data were previously available for the site.

The laboratory programme presented here provides new strength, failure, elastic and acoustic-property data for sandstone reservoir material from Stenlille. The tested material was obtained from Gassum Formation core recovered from the Stenlille-5, Stenlille-6, Stenlille-13 and Stenlille-14 wells at the Stenlille site, Denmark. The testing was designed to characterise the mechanical response of five sandstone types under drained triaxial conditions representative of the stress and pore pressure conditions relevant to the sampled intervals. P-wave and fast and slow S-wave (S1 and S2) velocities were also measured at selected stages during loading to characterise their evolution with changing stress conditions, calculate corresponding dynamic elastic properties, and evaluate elastic anisotropy.

Where sufficient material was available, plugs within each sandstone type were selected from the same well and a comparable depth interval to reduce sample variability. Sandstone Type 5 was the exception because insufficient suitable material was available from a single well. his group therefore includes material of the same lithology from both Stenlille-5 and Stenlille-6. Three plugs from each sandstone type were tested at different effective confining pressures to provide multiple failure measurements from which a Mohr-Coulomb failure envelope could be defined. The Mohr-Coulomb failure criterion was selected as the primary framework for evaluating the failure behaviour of the sandstone groups because it provides a simple and widely used representation of pressure-dependent rock strength in terms of cohesion and friction and allows an equivalent unconfined compressive strength (UCS) to be estimated from confined triaxial test data.

The subsequent sections describe the tested samples and basis for selection of the test conditions (Section 2), outline the experimental procedure (Section 3), present the methods used to calculate effective stress, static and dynamic elastic properties and Mohr-Coulomb failure parameters (Section 4), and present the mechanical and acoustic results for each sandstone type (Section 5).

2 Sample Preparation & Experimental Setup

Each sample was positioned between two hardened-steel end platens, both prepared with rubber membranes, and jacketed with heat-shrink polytetrafluoroethylene (PTFE) material. Stainless-steel lockwires (0.81 mm) were used to secure the seals at the PTFE and rubber-membrane interfaces. The hardened-steel end platens were equipped with internal piezoelectric transducers (PZTs), which allowed for acoustic velocity measurements during active testing. One PZT was aligned parallel to the loading direction for compressional wave (P-wave) arrivals, while the other two were oriented orthogonally to measure the fast and slow shear wave arrivals (S1 and S2).

The test plugs were supplied in a partially to fully water saturated condition. The initial degree of saturation, however, was not independently verified. The initial masses reported here are therefore reported as as-received, pre-test values rather than as formally determined saturated masses. Most test plugs had lengths of 106.22–113.99 mm and diameters of 53.10–54.15 mm, giving length-to-diameter (L/D) ratios of 1.98–2.11. These ratios were broadly consistent with the specimen geometry recommended in the ISRM Suggested Methods (ISRM, 2007). Two shorter specimens fell outside this range. Plug 30 had a length of 99.02 mm and an L/D ratio of 1.86, while Plug 34 had a length of 87.40 mm and an L/D ratio of 1.62. Plug 34 was re-prepared

at the shorter length because the original sample was chipped. The sample details, as-received masses, and dimensions are summarised in Table 1.

The jacketed sample assembly was instrumented with two internal axial extensometers (MTS 632.90F-12), positioned centrally along the sample axis, and one circumferential chain extensometer (MTS 632.92H-03), mounted at the midpoint between the axial extensometers.

Mechanical testing was performed using a servo-controlled triaxial apparatus (MTS 815 rock test system) in the BGS Rock Mechanics and Physics Laboratory (Figure 1). The apparatus consists of a stiff load frame with a maximum axial load of 4600 kN and a confining pressure chamber rated to 140 MPa and 200 °C. The instrumented sample stack was positioned within the confining pressure chamber, with an internal thermocouple placed near the sample to monitor temperature. Axial load was measured by an internal load cell (MTS 661.98B.01) seated above the assembly, while inert mineral oil was used as the confining medium.



Figure 1. Triaxial setup for the MTS 815 rock test system at the British Geological Survey.

Calibration of the load cell, axial extensometers, and circumferential extensometer is performed annually by MTS Systems Ltd, an ISO-accredited service provider. A calibration report and certificate are issued following each calibration cycle. These procedures ensure that the instrumentation meets the requirements of BS EN ISO 9513:2012 and BS EN ISO 7500-1:2018. Load cell calibrations are embedded in the MTS 793 MultiPurpose TestWare software so that output files contain corrected force measurements.

3 Experimental Programme & Procedure

3.1 SAMPLE SELECTION, TEST CONDITIONS, & PORE FLUID CHEMISTRY

The testing programme consisted of 15 drained triaxial compressive strength tests, with three tests completed for each of five sandstone types. The plugs were grouped primarily by assigned sandstone lithology and, where sufficient material was available, by well and comparable logging depth. Sandstone Types 1-4 each comprised three plugs from the same well over a relatively narrow depth interval (Table 1). For Sandstone Type 5, insufficient suitable material was available from Stenlille-5 to complete the triplicate test set, so Plug 35 from Stenlille-6 was used because it had the same assigned lithology and a broadly comparable logging depth. Similar measured depths in different wells do not necessarily represent the same stratigraphic position because of lateral variations in unit depth and thickness. The use of material from two wells within Sandstone Type 5 may therefore introduce additional sample variability within this group.

Table 1 Sample information for the sandstone material used in the triaxial testing programme.

Sample ID	Sandstone Type	Well	Depth (MD)	Length (mm)	Diameter (mm)	Weight as-received (g)	L:D ratio (-/-)
Plug 22	Sandstone Type 1	Stenlille-5	1580.93	110.16	54.07	562.88	2.04
Plug 21	Sandstone Type 1	Stenlille-5	1580.79	113.90	54.15	578.79	2.10
Plug 23	Sandstone Type 1	Stenlille-5	1581.10	113.99	53.98	585.96	2.11
Plug 25	Sandstone Type 2	Stenlille-14	1684.52	113.32	53.74	550.39	2.11
Plug 26	Sandstone Type 2	Stenlille-14	1685.28	111.16	53.57	558.27	2.08
Plug 27	Sandstone Type 2	Stenlille-14	1685.47	109.67	53.66	553.51	2.04
Plug 33	Sandstone Type 3	Stenlille-6	1582.48	110.79	53.40	552.81	2.07
Plug 32	Sandstone Type 3	Stenlille-6	1581.88	109.55	53.80	553.13	2.04
Plug 34	Sandstone Type 3	Stenlille-6	1584.63	87.40	53.83	441.84	1.62
Plug 31	Sandstone Type 4	Stenlille-13	1719.87	108.34	53.46	530.95	2.03
Plug 10	Sandstone Type 4	Stenlille-13	1717.40	110.08	53.10	536.18	2.07
Plug 30	Sandstone Type 4	Stenlille-13	1718.87	99.02	53.32	486.49	1.86
Plug 35	Sandstone Type 5	Stenlille-6	1574.50	106.22	53.76	—	1.98
Plug 11	Sandstone Type 5	Stenlille-5	1570.95	113.38	53.69	574.75	2.11
Plug 12	Sandstone Type 5	Stenlille-5	1571.20	111.44	53.68	565.11	2.08

Vertical stress profiles derived from integration of well log density data were provided by GEUS (see Appendix 2). The logging depth of each plug was matched to the nearest corresponding depth in the relevant profile to estimate the in-situ total vertical stress for that sample. The total vertical stress estimates were similar for the three plugs within each sandstone group and were rounded to define a representative in-situ stress condition for testing. One test within each group was conducted at a confining pressure corresponding approximately to this value, while the remaining two tests were conducted at lower confining pressures to provide additional failure points for the Mohr-Coulomb analysis. The resulting test conditions are summarised in Table 2.

A pore pressure of 16 MPa was maintained during testing. Synthetic brine was used as the pore fluid medium to replicate the in-situ pore-fluid chemistry and minimise potential rock to fluid interactions that could arise if a generic laboratory fluid were used. The brine composition was based on formation water from the Gassum Formation in the Stenlille-18 well at 1662 m. The

resulting recipe has a total dissolved solids concentration of 186,032.473 mg/L, an estimated density of 1.1188 g/mL at 20 °C, a calculated salinity of 16.627 wt%, and an NaCl-equivalent concentration of 3.18 mol/L. The principal-ion composition is provided in Appendix 1.

Table 2 Test conditions for each drained triaxial compressive strength test. Depth-vertical stress profiles were derived from well log data was provided by GEUS. The logging depth of each sample was matched to this profile to estimate the corresponding in situ vertical stress. For each sandstone type, one of the three tests was conducted at a confining pressure representative of this estimated in situ vertical stress. The remaining two tests from each triplicate set were conducted at lower confining pressures to constrain the Mohr-Coulomb failure envelope.

Sample ID	Sandstone Type	Well	Depth (MD)	Estimated vertical stress (MPa)	Confining pressure (MPa)	Pore pressure (MPa)	Effective confining pressure (MPa)
Plug 22	Sandstone Type 1	Stenlille-5	1580.93	35.42	35	16	19
Plug 21	Sandstone Type 1	Stenlille-5	1580.79	35.41	30	16	14
Plug 23	Sandstone Type 1	Stenlille-5	1581.10	35.42	25	16	9
Plug 25	Sandstone Type 2	Stenlille-14	1684.52	34.21	34	16	18
Plug 26	Sandstone Type 2	Stenlille-14	1685.28	34.22	29	16	13
Plug 27	Sandstone Type 2	Stenlille-14	1685.47	34.23	24	16	8
Plug 34	Sandstone Type 3	Stenlille-6	1584.63	36.23	36	16	20
Plug 33	Sandstone Type 3	Stenlille-6	1582.48	36.19	31	16	15
Plug 32	Sandstone Type 3	Stenlille-6	1581.88	36.17	26	16	10
Plug 31	Sandstone Type 4	Stenlille-13	1719.87	34.43	34	16	18
Plug 10	Sandstone Type 4	Stenlille-13	1717.40	34.38	29	16	13
Plug 30	Sandstone Type 4	Stenlille-13	1718.87	34.41	24	16	8
Plug 35	Sandstone Type 5	Stenlille-6	1574.50	36.01	36	16	20
Plug 11	Sandstone Type 5	Stenlille-5	1570.95	35.20	31	16	15
Plug 12	Sandstone Type 5	Stenlille-5	1571.20	35.20	26	16	10

3.2 EXPERIMENTAL PROCEDURE

Before pressurisation, an initial axial stress of 1 MPa was applied to establish contact between the sample and end platens. Axial and circumferential deformation were measured continuously throughout testing using the internal extensometers described in Section 1. The pore pressure pump was connected to the base of the sample assembly and synthetic brine was introduced from the base while the upper pore pressure outlet remained open to atmospheric conditions. Flow was continued until pore fluid was observed at the upper outlet, after which the outlet was sealed, and the pore pressure intensifier was stopped. The confining pressure chamber was then sealed and filled with the confining fluid.

Confining pressure and pore pressure were subsequently increased simultaneously at rates of 1 MPa/min and 0.5 MPa/min, respectively, until the target confining pressure for each test (Table 2) and a pore pressure of 16 MPa were reached. These conditions were held for a minimum of 3 hours, or until the axial and radial strain measurements indicated that the sample response had equilibrated. Following equilibration, axial loading was applied at a constant axial strain rate of 5×10^{-6} s^{-1} under drained conditions while keeping the target confining and pore pressures constant (ISRM, 2007). Axial loading was continued sample failure occurred, after which the sample was allowed to shear further until a steady-state residual stress was reached.

P-wave and fast and slow S-wave (S1 and S2) velocities were measured at regular intervals during axial loading to characterise their evolution with changing stress conditions.

Measurements were generally acquired at 5 MPa increments in differential stress during earlier loading, increasing to approximately 10 MPa increments at higher stresses.

Mechanical data from the MTS system were recorded in both the time and force domains. Time-domain data were recorded at 2 Hz, while force-domain acquisition recorded an additional data point for each 250 N change in axial force. This additional acquisition ensured that changes in force occurring between the predefined time-domain sampling intervals were captured. Pore pressure and pore volume data were recorded independently at 1 Hz by the pore pressure system. The MTS time-domain data, MTS force-domain data, and pore-pressure data were subsequently combined during post-test data processing.

Once a steady-state residual stress had been reached, the differential stress was reduced to zero to return the sample to hydrostatic stress conditions. Confining pressure and pore pressure were then reduced to zero at a rate of 1 MPa/min. Following complete depressurisation and unloading, the sample was removed from the pressure vessel for post-test examination and analysis.

4 Mechanical Property & Failure Analysis

4.1 STRESS, STRAIN, & PEAK STRENGTH

In triaxial tests, the intermediate and minor principal stresses were equal to the applied confining pressure ($\sigma_2 = \sigma_3$). For the MTS 815 configuration used here, the confining pressure also contributed to the total axial stress, with the loading piston applying an additional axial force during loading. The total axial stress, which corresponds to the major principal stress (σ_1), was therefore calculated as:

$$\sigma_1 = P_C + \sigma_d \tag{1}$$

Where P_C is the applied confining pressure and σ_d is the differential stress. Differential stress was calculated from the axial force applied from the piston and initial cross-sectional area of the sample:

$$\sigma_d = \frac{F}{A} \tag{2}$$

Where F is the applied axial force and A is the cross-sectional area of the sample. Since the tests were conducted at a controlled pore pressure, the effective major and minor principal stresses were defined as the difference between the corresponding total principal stress and pore pressure (P_f):

$$\sigma_1' = \sigma_1 - P_f \tag{3}$$

$$\sigma_3' = P_C - P_f \tag{4}$$

Where σ_1' and σ_3' are the effective major and minor principal stresses, respectively.

Axial strain was measured using the two internal axial extensometers, with the average response used for the subsequent analysis. Radial strain was determined from the circumferential deformation measured by the internal chain extensometer. The axial stress and corresponding axial and radial strain measurements were used to determine the static elastic parameters described in section 3.2.

The peak effective axial stress was defined as the maximum effective axial stress reached during active loading. The peak effective axial stress and corresponding effective confining pressure values from each test within a triplicate set were then used to define the Mohr-Coulomb failure relationship for each sandstone type, as described in Section 3.3.

4.2 STATIC ELASTIC PARAMETERS

Static Young's modulus (E) and Poisson's ratio (v) were determined from the stress and strain measurements described in Section 3.1. A linear fitting interval was selected from the pre-failure stress-strain response within approximately 30-50% of the peak effective axial stress. The same interval was used to calculate both the static Young's modulus and Poisson's ratio.

Young's modulus was determined from the slope of a linear fit to the effective axial stress and axial strain data over the selected fitting interval:

$$E = \frac{\Delta\sigma_1'}{\Delta\varepsilon_a} \tag{5}$$

Where $\Delta\sigma_1'$ is the change in effective axial stress over the fitting interval and $\Delta\varepsilon_a$ is the corresponding change in the average axial strain. As the axial stress is reported in megapascals (MPa), a conversion factor was applied to the calculated Young's modulus and reported in gigapascals (GPa).

Poisson's ratio was determined from the relationship between the radial and average axial strain over the same fitting interval:

$$v = \frac{\Delta\varepsilon_r}{\Delta\varepsilon_a} \tag{6}$$

Where $\Delta\varepsilon_r$ is the change in radial strain. The sign convention was applied such that radial expansion during axial compression resulted in a positive Poisson's ratio value.

4.3 MOHR-COULOMB FAILURE ANALYSIS

The Mohr-Coulomb failure analysis used the peak effective axial stress and corresponding effective confining pressure values from each test to characterise the pressure-dependent failure behaviour of each sandstone type. The relationship between the peak effective axial stress and effective confining pressure was then determined using a least-squares linear fit in effective stress space:

$$\sigma_1' = m\sigma_3' + b \tag{7}$$

Where m is the slope of the fitted failure relationship and b is the intercept at zero effective confining pressure. This intercept corresponds to the estimated unconfined compressible strength (UCS). The slope was then used to calculate the friction coefficient (μ):

$$\mu = \frac{m - 1}{2\sqrt{m}} \tag{8}$$

The corresponding angle of internal friction (φ) was calculated as:

$$\varphi = \tan^{-1}(\mu) \tag{9}$$

Cohesion (c) was determined independently from the estimated UCS and slope of the fitted failure relationship:

$$c = \frac{UCS}{2\sqrt{m}} \tag{10}$$

The calculated friction coefficient and cohesion were then used to define the Mohr-Coulomb failure envelope in effective normal stress-shear stress space:

$$\tau = c + \mu\sigma_n' \tag{11}$$

Where τ is the shear stress and σ_n' is the effective normal stress.

Mohr circles were constructed from the peak effective axial stress (σ_1') and corresponding effective confining pressure (σ_3') for each test to represent stress conditions at failure relative to the fitted failure envelope. The centre (C) and radius (R) of each Mohr circle were calculated as:

$$C = \frac{\sigma_1' + \sigma_3'}{2} \tag{12}$$

$$R = \frac{\sigma_1' - \sigma_3'}{2} \tag{13}$$

The lower and upper bounds of each circle on the effective normal stress axis correspond to (σ_3') and (σ_1'), respectively. The shear stresses along the upper half of the circle were calculated for values of effective normal stress between these bounds as:

$$\tau = \sqrt{(R)^2 - (\sigma_n' - C)^2} \tag{14}$$

For Sandstone Types 1, 2, 4, and 5, all three peak strength values were included in the linear regression. For Sandstone Type 3, the three peak strength values did not define a consistent linear relationship with effective confining pressure. A linear fit to all three results produced a negative intercept at zero effective confining pressure and was therefore not considered physically meaningful for estimating UCS. Of the possible two-point combinations, only Plugs 32 and 33 produced a positive UCS intercept. These two tests were therefore used to determine the reported Mohr–Coulomb parameters for Sandstone Type 3. The resulting parameters are based on two triaxial tests and should be used with caution.

4.4 ACOUSTIC VELOCITIES & DYNAMIC ELASTIC PARAMETERS

Compressional (P-wave) and fast- and slow-shear wave (S1 & S2) travel times were measured during testing and combined with the sample length to calculate the corresponding acoustic velocities:

$$V = \frac{L}{t} \tag{15}$$

Where V is the acoustic velocity, L is the sample length, and t is the corrected travel time through the sample. Since the measured travel times include propagation through both the sample and the endcap sections of the sample assembly, the travel time component associated with these endcaps was removed before calculating the final velocity values. This provided pressure-dependent P-wave (V_P), fast S-wave (V_{S1}), and slow S-wave (V_{S2}) velocity trends during loading for each sample.

The measured P-wave and fast S-wave velocities were used together with sample density (ρ) to calculate the isotropic-equivalent dynamic elastic parameters using standard elastic relationships. The orthogonally polarised slow S-wave velocity was reported together with V_{S1} to evaluate shear-wave splitting and its evolution with changing stress conditions.

The reported dynamic Young's modulus (E_{dyn}) and Poisson's ratio (v_{dyn}) were calculated from V_P, V_{S1}, and ρ as follows:

$$E_{dyn} = \rho V_{S1}^2 \left(\frac{3V_P^2 - 4V_{S1}^2}{V_P^2 - V_{S1}^2} \right) \tag{16}$$

$$v_{dyn} = \left(\frac{V_P^2 - 2V_{S1}^2}{2(V_P^2 - V_{S1}^2)} \right) \tag{17}$$

Dynamic bulk modulus (K_{dyn}) and shear modulus (G_{dyn}) were similarly calculated as:

$$K_{dyn} = \rho\left(V_P^2 - \frac{4}{3}V_{S1}^2\right) \quad (18)$$

$$G_{dyn} = \rho V_{S1}^2 \quad (19)$$

The dynamic elastic parameters represent the small strain elastic response derived from the acoustic wave propagation and differ from the static Young's modulus and Poisson's ratio determined from the mechanical stress-train response described in Section 3.2. Acoustic measurements involve very small strain increments applied over a short timescale and, for saturated samples, can be considered effectively undrained. In contrast, the static elastic parameters were determined over a larger stress and strain interval during drained mechanical loading. Dynamic Young's modulus is commonly greater than its static counterpart because the two measurements represent substantially different strain amplitudes, loading frequencies, and drainage conditions.

The difference between the two orthogonally polarised shear-wave velocities was also evaluated using a percentage velocity contrast. The calculation and corresponding results are provided in Appendix 3.

5 Results

5.1 MECHANICAL RESULTS

The strength and static elastic properties determined from the 15 drained triaxial compressive strength tests are summarised in Table 3. Effective confining pressures ranged from 8 to 20 MPa, with peak effective axial stresses ranging from 58.48 to 145.07 MPa.

The stress-strain curves showed the typical deformation response associated with triaxial compression. Initial non-linear deformation was associated with closure of pre-existing cracks and pore space, followed by an approximately linear elastic region. Departure from the linear response marked the onset of yielding, which is associated with crack initiation and stable crack growth. With further loading, the samples progressed towards unstable crack growth and localisation before reaching peak strength and subsequent sample failure. Post-peak deformation was characterised by strain softening and progression towards residual shearing (Nicksiar & Martin, 2012; Naderloo et al., 2023).

It is worth noting that, although the deformation stages described above can be characterised using individual crack initiation and crack damage stress thresholds, these thresholds were not determined for the current tests. Peak effective axial stress was the only strength threshold quantified in this analysis. Static Young's modulus and Poisson's ratio were determined over the same fitting interval within the linear elastic region of each loading curve, using the effective axial stress-axial strain and radial strain-axial strain relationships, respectively.

Static Young's modulus ranged from 10.55 to 18.16 GPa, while static Poisson's ratio values of 0.0012 to 0.414. The Poisson's ratio results showed more variability than the Young's modulus values, including particularly low values of 0.0012 and 0.018 for Plugs 34 and 31, respectively.

The Mohr-Coulomb failure parameters derived for each sandstone type are summarised in Table 4. Estimated unconfined compressive strength (UCS) values ranged from 21.41 to 60.27 MPa, cohesion from 4.75 to 17.07 MPa, and friction angle from 20.37° to 42.14°. Sandstone Type 1 had the highest estimated UCS and cohesion, while Sandstone Type 3 had the lowest UCS and cohesion and the highest friction angle. It should be noted, however, that the parameters for Sandstone Type 3 were derived from two tests and should be treated with caution.

Table 3 Summary of the Stenlille drained triaxial test results. Mohr-Coulomb failure parameters are shown for each sandstone type. The parameters for Sandstone Type 3 are based on Plugs 32 and 33 only and should be used with caution.

Sample ID	Sandstone Type	Effective confining pressure (MPa)	Peak effective axial stress (MPa)	Static Young's Modulus (GPa)	Static Poisson's Ratio (-/-)
Plug 22	Sandstone Type 1	19	121.34	16.24	0.150
Plug 21	Sandstone Type 1	14	100.15	13.71	0.143
Plug 23	Sandstone Type 1	9	90.18	10.55	0.179
Plug 25	Sandstone Type 2	18	95.24	13.85	0.173
Plug 26	Sandstone Type 2	13	83.11	14.48	0.148
Plug 27	Sandstone Type 2	8	66.17	13.08	0.197
Plug 34	Sandstone Type 3	20	145.07	18.16	0.0012
Plug 33	Sandstone Type 3	15	97.57	15.52	0.070
Plug 32	Sandstone Type 3	10	72.19	16.87	0.414
Plug 31	Sandstone Type 4	18	79.16	13.51	0.018
Plug 10	Sandstone Type 4	13	73.93	13.72	0.156
Plug 30	Sandstone Type 4	8	58.48	12.65	0.206
Plug 35	Sandstone Type 5	20	127.75	16.38	0.126
Plug 11	Sandstone Type 5	15	104.60	16.77	0.102
Plug 12	Sandstone Type 5	10	85.68	16.26	0.162

Table 4 Summary of the Mohr-Coulomb failure parameters for each sandstone type. Note that the parameters for Sandstone Type 3 are based on Plugs 32 and 33 only and should be used with caution.

Sandstone Type	Estimated UCS (MPa)	Cohesion (MPa)	Friction angle (°)	Friction coefficient (-/-)
Sandstone Type 1	60.27	17.07	30.93	0.599
Sandstone Type 2	43.72	12.82	29.21	0.559
Sandstone Type 3	21.41	4.75	42.14	0.904
Sandstone Type 4	43.46	15.17	20.37	0.371
Sandstone Type 5	42.90	10.45	38.02	0.781

Across the test programme, increasing effective confining pressure was consistently associated with an increase in peak effective axial stress. The post-peak response also varied with confining pressure, with tests conducted at higher confining pressures usually resulting in higher residual strength. This behaviour is consistent with the expected transition towards less brittle (i.e., ductile) deformation with increasing confining pressure.

5.1.1 Sandstone Type 1

The mechanical response of Sandstone Type 1 at effective confining pressures of 9, 14, and 19 MPa is shown in Figure 2. Peak effective axial stress increased from 90.18 MPa to 121.34 MPa as effective confining pressure increased from 9 to 19 MPa, with an intermediate peak strength of 100.15 MPa at 14 MPa effective confining pressure. Following peak strength, all three samples showed strain softening behaviour that evolved towards a constant residual stress value. The highest confining pressure test (i.e., Plug 22) showed a smaller post-peak stress reduction in comparison to the tests conducted at lower effective confining pressures. This

behaviour is consistent with the expected transition towards less brittle deformation with increasing confining pressure.

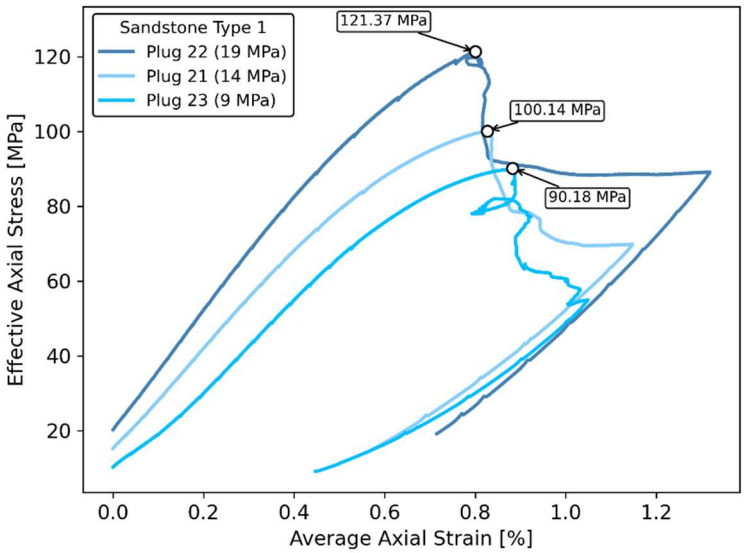


Figure 2. Effective axial stress and axial strain response of the three Sandstone Type 1 samples.

Static Young's modulus increased from 10.55 to 16.24 GPa across the three tests as effective confining pressure increased. Poisson's ratio ranged from 0.143 to 0.179 and showed no systematic change with effective confining pressure (Table 3). The peak strength results were used to characterise the Mohr-Coulomb failure behaviour of Sandstone Type 1. Peak effective axial stress increased linearly with effective confining pressure (Figure 3). Extrapolation of the linearly fitted relationship to zero effective confining pressure gave an estimated UCS of 60.27 MPa.

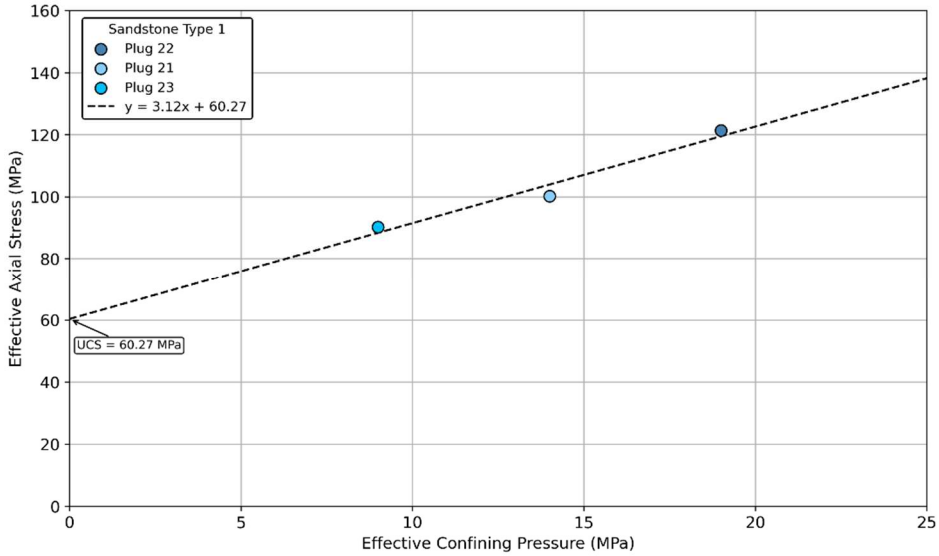


Figure 3. Relationship between peak effective axial stress and effective confining pressure for Sandstone Type 1. The dashed line shows the linear fit to the three test results, with extrapolation to zero effective confining pressure used to estimate UCS.

The corresponding Mohr-Coulomb failure envelope (Figure 4) gave a cohesion of 17.07 MPa and friction angle of 30.93° (Table 4).

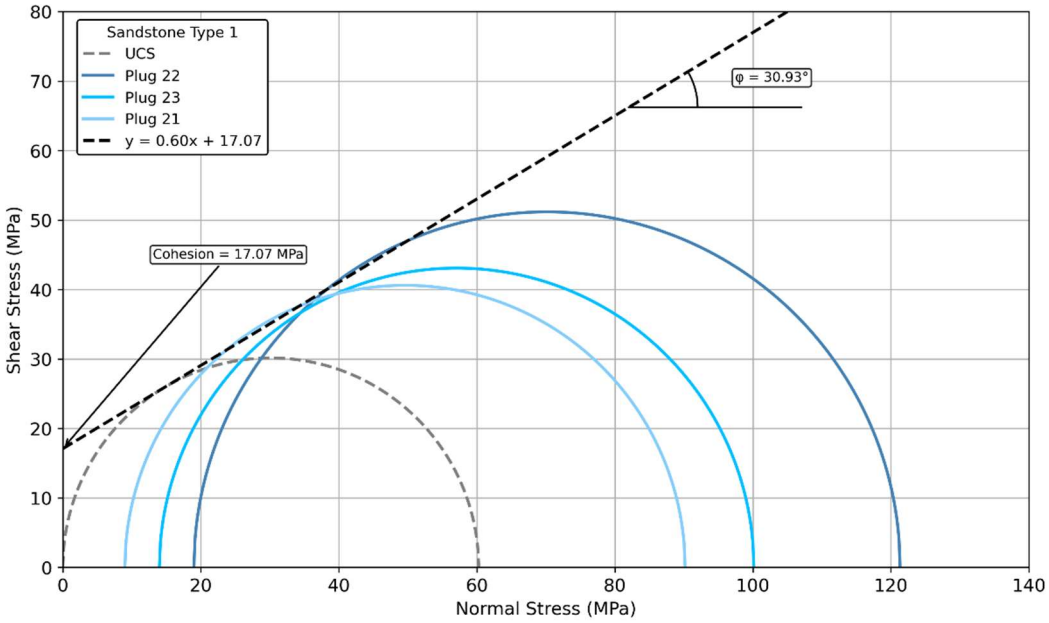


Figure 4. Mohr-Coulomb failure analysis for Sandstone Type 1. Mohr circles are shown for the three drained triaxial tests, together with the fitted failure envelope and extrapolated UCS circle.

5.1.2 Sandstone Type 2

Sandstone Type 2 was tested at effective confining pressures of 8, 13, and 18 MPa, with the resulting stress-strain behaviour shown in Figure 5. Peak effective axial stress increased from 66.17 to 95.24 MPa as effective confining pressure increased from 8 to 18 MPa, with an intermediate peak strength of 83.11 MPa at 13 MPa effective confining pressure.

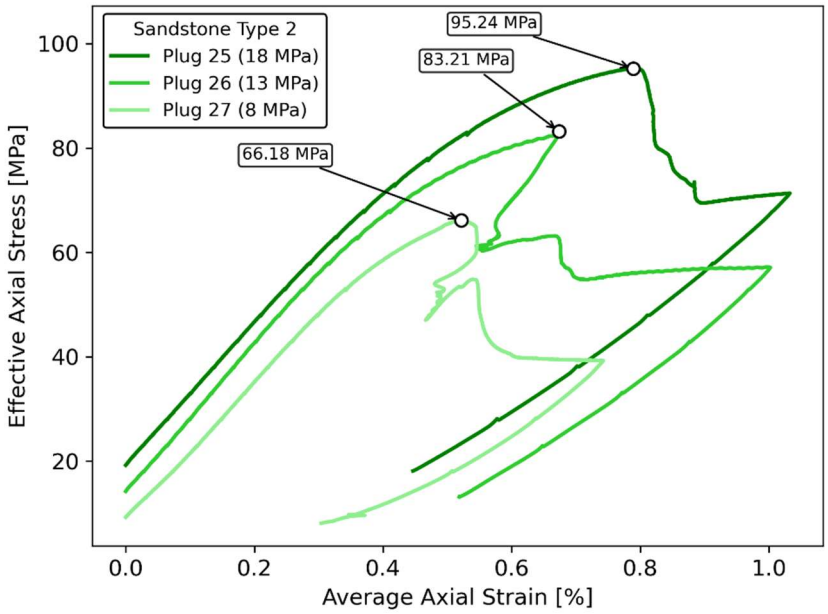


Figure 5. Effective axial stress and axial strain response of the three Sandstone Type 2 samples.

Sandstone Type 2 showed similar post-peak behaviour to Sandstone Type 1, with all three samples showing strain softening and an evolution towards a constant residual stress state. The tests conducted at higher effective confining pressures showed a smaller post-peak stress reduction when compared with the lowest confining pressure test. This behaviour is again consistent with the expected transition towards less brittle deformation with increasing confining pressure.

In contrast to Sandstone Type 1, Static Young's modulus showed no systematic increase with effective confining pressure and ranged from 13.08 to 14.48 GPa. Poisson's ratio ranged from

0.148 to 0.197 and also showed no systematic change with effective confining pressure (Table 3).

The peak strength results were used to as inputs to the Mohr-Coulomb failure criterion for Sandstone Type 2. Peak effective axial stress increased linearly with effective confining pressure (Figure 6).

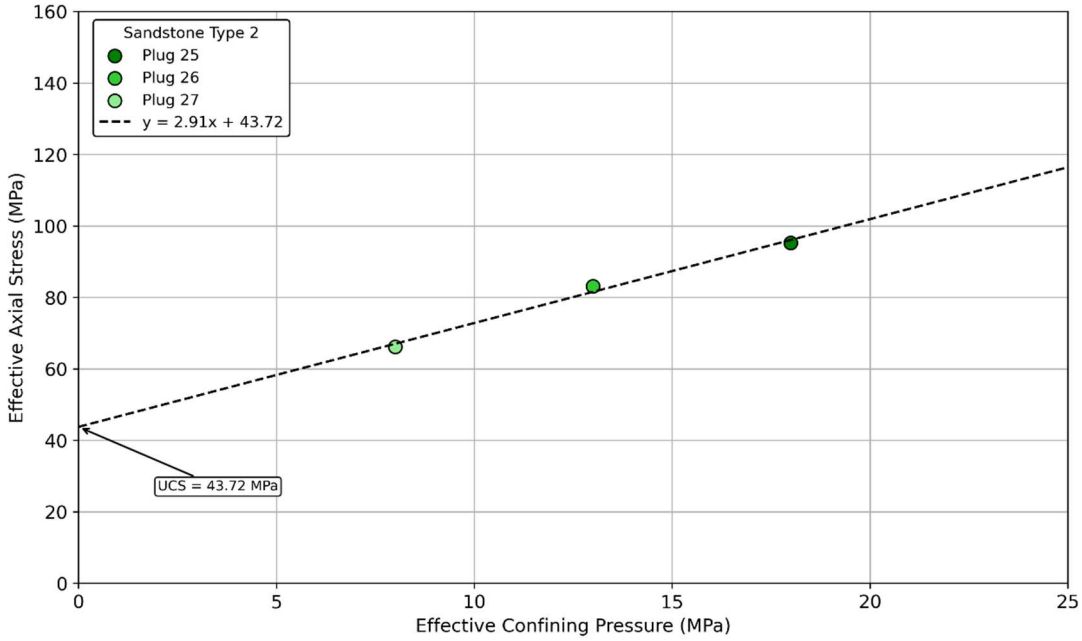


Figure 6. Relationship between peak effective axial stress and effective confining pressure for Sandstone Type 2. The dashed line shows the linear fit to the three test results, with extrapolation to zero effective confining pressure used to estimate UCS.

Extrapolation of the linear relationship to zero effective confining pressure resulted in an estimated UCS of 43.72 MPa. The corresponding Mohr-Coulomb failure envelope (Figure 7) gave a cohesion of 12.82 MPa and friction angle of 29.21° (Table 4).

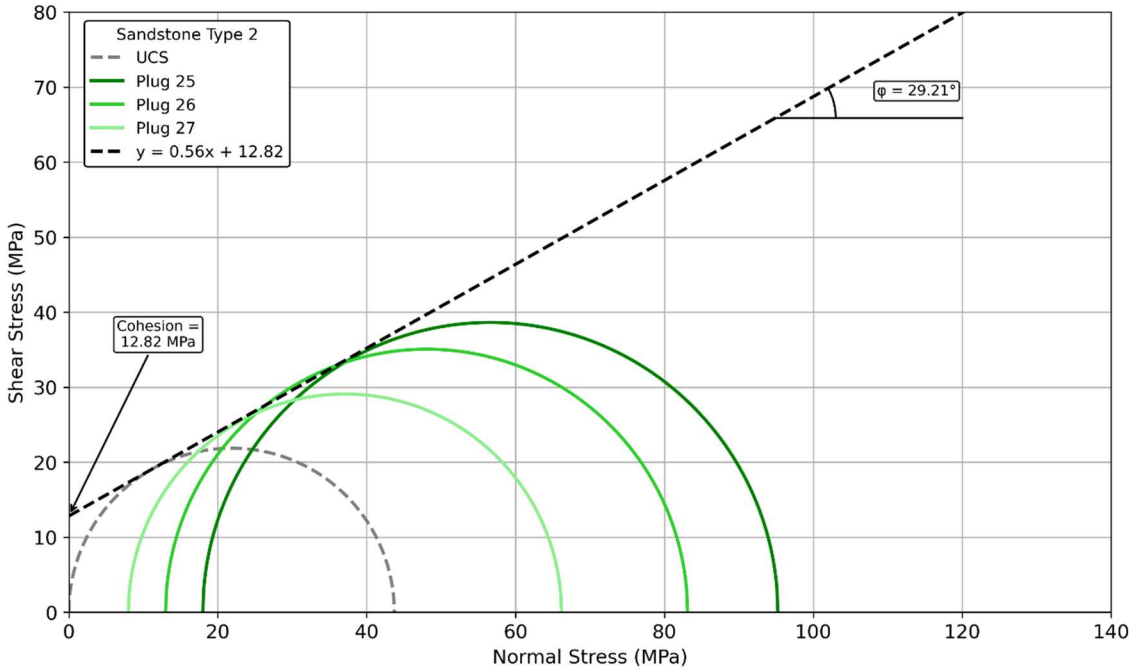


Figure 7. Mohr-Coulomb failure analysis for Sandstone Type 2. Mohr circles are shown for the three drained triaxial tests, together with the fitted failure envelope and extrapolated UCS circle.

5.1.3 Sandstone Type 3

Sandstone Type 3 was tested at effective confining pressures of 10, 15, and 20 MPa, with the resulting stress-strain behaviour shown in Figure 8. Peak effective axial stress increased from 72.19 to 145.07 MPa as effective confining pressure increased from 10 to 20 MPa. An intermediate peak strength of 97.57 MPa was measured at 15 MPa effective confining pressure. The two lower confining pressure tests showed post-peak strain softening broadly similar to Sandstone Types 1 and 2. Plug 34, however, reached a substantially higher peak effective axial stress value of 145.07 MPa at 20 MPa effective confining pressure.

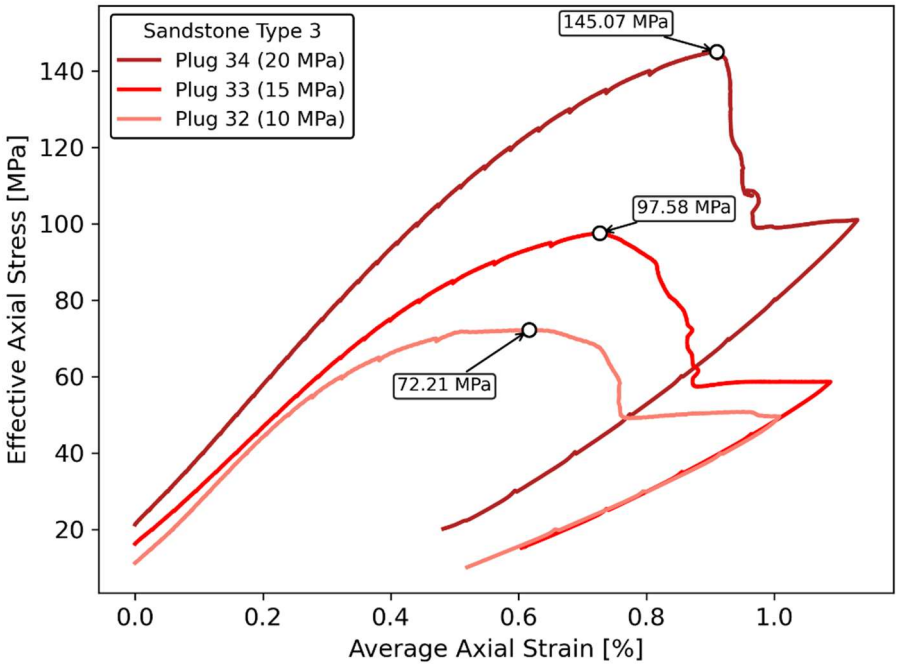


Figure 8. Effective axial stress and axial strain response of the three Sandstone Type 3 samples.

Static Young's modulus ranged from 15.52 to 18.16 GPa and showed no systematic change with effective confining pressure. These values were generally higher than those obtained for Sandstone Types 1 and 2. Poisson's ratio showed greater variation, with values of 0.414, 0.070, and 0.0012 for Plugs 32, 33, and 34, respectively (Table 3). The near-zero value obtained for Plug 34 is unlikely to represent the radial deformation behaviour of the sample and may indicate an issue with the circumferential strain measurement. In contrast, the value of 0.414 obtained for Plug 32 is physically plausible but notably higher than the other Poisson's ratio measurements obtained during the test programme.

The peak strength results from Plugs 32 and 33 were used to characterise the failure behaviour of Sandstone Type 3 using the Mohr-Coulomb failure criterion. The two failure points define the fitted relationship shown in Figure 9. Extrapolation of this relationship to zero effective confining pressure gave an estimated UCS of 21.41 MPa. The corresponding Mohr-Coulomb failure envelope (Figure 10) gave a cohesion of 4.75 MPa and friction angle of 42.14° (Table 4).

The three Sandstone Type 3 tests did not define a consistent linear relationship between peak strength and effective confining pressure. Plug 34 produced an unusually high peak strength relative to the other tests and was excluded from the reported Mohr-Coulomb fit. The available data are insufficient to determine which of the three results accounts for the departure from linear behaviour. It is worth noting, however, that of the possible combinations only Plugs 32 and 33 produced a positive UCS estimate. Nevertheless, the relatively high friction angle obtained from this combination introduces further uncertainty regarding the reliability of the fitted failure parameters. Repeat testing would be required to resolve this uncertainty, and the resulting Mohr-Coulomb failure parameters for Sandstone Type 3 should therefore be treated with caution.

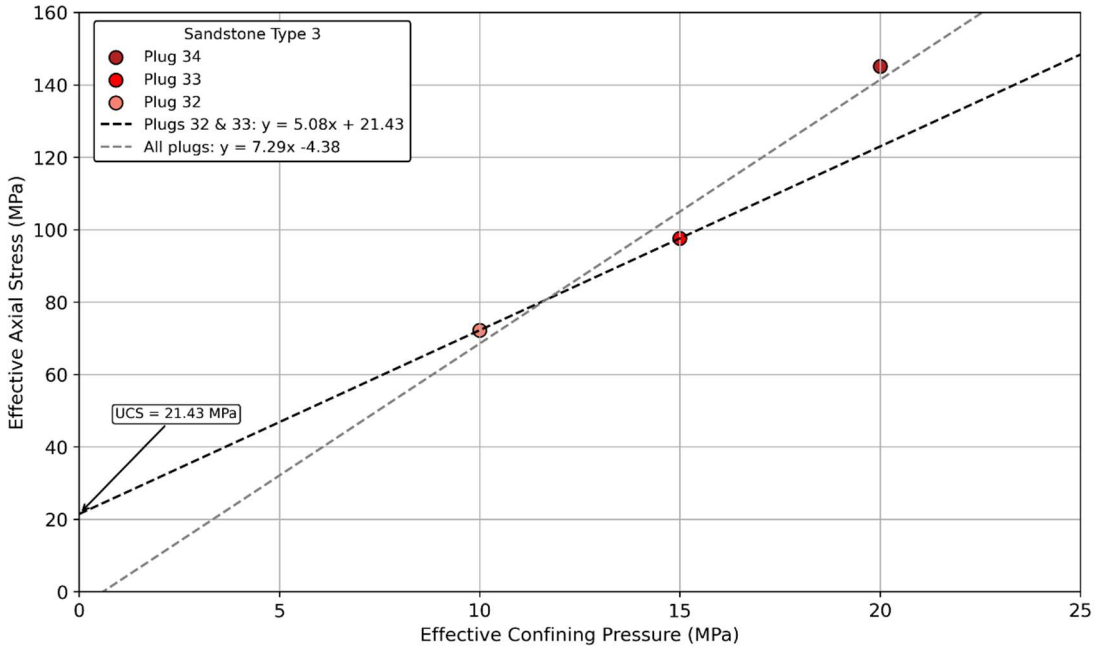


Figure 9. Relationship between peak effective axial stress and effective confining pressure for Sandstone Type 3. The black dashed line shows the linear fit to Plugs 32 and 33 used to determine the reported Mohr-Coulomb parameters. The grey dashed line shows the linear fit to all three test results, which produces a negative intercept at zero effective confining pressure.

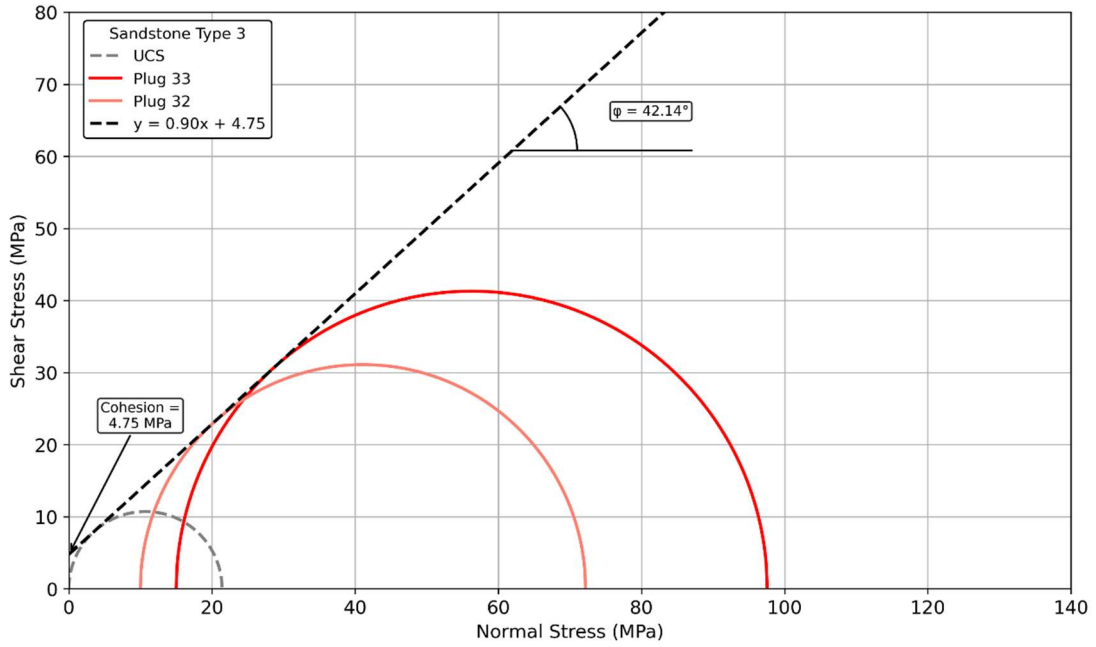


Figure 10. Mohr-Coulomb failure analysis for Sandstone Type 3. Mohr circles are shown for the tests conducted on Plugs 32 and 33, together with the fitted failure envelope and extrapolated UCS circle.

5.1.4 Sandstone Type 4

The stress-strain behaviour of Sandstone Type 4 at effective confining pressures of 8, 13, and 18 MPa is shown in Figure 11. Peak effective axial stress increased from 58.48 to 79.16 MPa as effective confining pressure increased from 8 to 18 MPa. An intermediate peak strength of 73.93 MPa was measured at 13 MPa effective confining pressure.

Similar to Sandstone Types 1 and 2, all three samples showed post-peak strain softening and an evolution towards a residual stress value. The highest confining pressure test (i.e., Plug 31) showed the smallest post-peak stress reduction, consistent with the transition towards less brittle deformation with increasing confining pressure.

Static Young's modulus showed little variation with effective confining pressure and ranged from 12.65 to 13.72 GPa, which is similar to the range obtained for Sandstone Type 2. Poisson's ratio values of 0.156 and 0.206 were estimated for Plugs 10 and 30, respectively, while Plug 31 gave a lower value of 0.018 (Table 3). The unusually low value for Plug 31 may reflect either uncertainty in the circumferential strain measurement or sample specific behaviour associated with local heterogeneity.

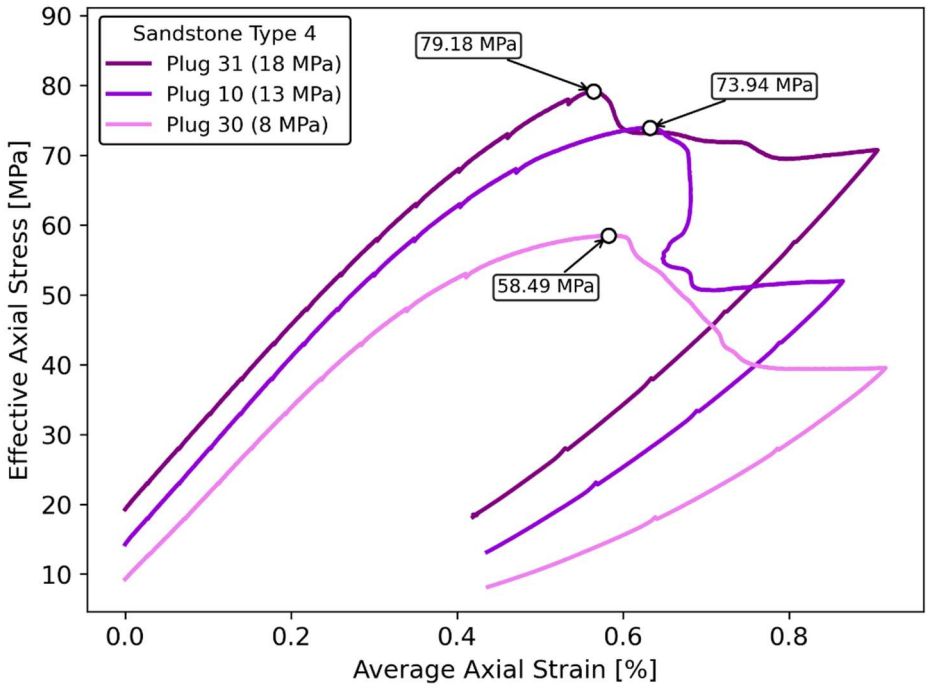


Figure 11. Effective axial stress and axial strain response of the three Sandstone Type 4 samples.

The peak strength results were used to determine the Mohr-Coulomb failure parameters for Sandstone Type 4. Peak effective axial stress increased approximately linearly with effective confining pressure (Figure 12).

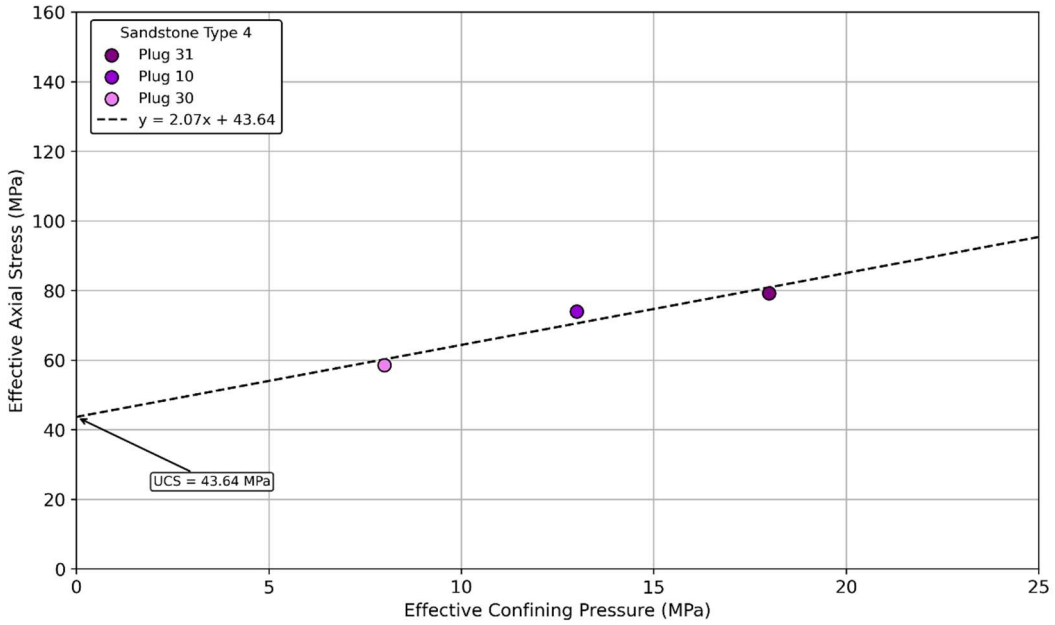


Figure 12. Relationship between peak effective axial stress and effective confining pressure for Sandstone Type 4. The dashed line shows the linear fit to the three test results, with extrapolation to zero effective confining pressure used to estimate UCS.

This relationship was extrapolated to zero effective confining pressure resulted in an estimated UCS of 43.46 MPa, which is in line with the 43.72 MPa estimated for Sandstone Type 2. The Mohr-Coulomb failure analysis (Figure 13) resulted in a cohesion of 15.17 MPa and friction angle of 20.37° (Table 4).

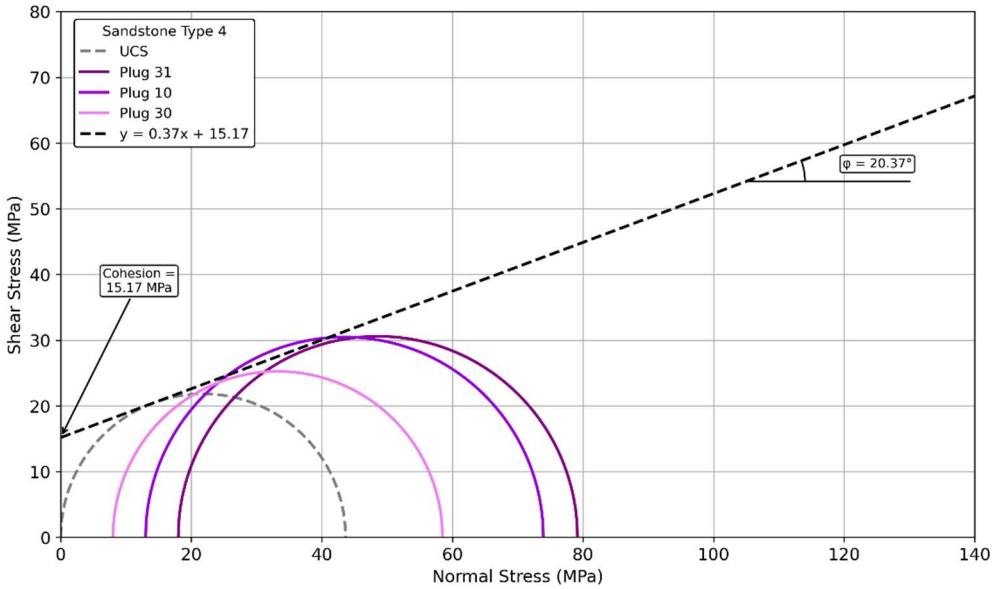


Figure 13. Mohr-Coulomb failure analysis for Sandstone Type 4. Mohr circles are shown for the three drained triaxial tests, together with the fitted failure envelope and extrapolated UCS circle.

5.1.5 Sandstone Type 5

Sandstone Type 5 was tested at effective confining pressures of 10, 15, and 20 MPa, with the resulting stress-strain behaviour shown in Figure 14. Peak effective axial stress increased from 85.68 to 104.60 to 127.75 MPa as effective confining pressure increased from 10 to 15 to 20 MPa, respectively. The samples showed similar post-peak behaviour as seen in Sandstone Types 1 and 2, with strain softening that evolved towards a constant residual stress state. The magnitude of stress reduction associated with the evolution towards the residual stress state decreased with increasing effective confining pressure. This behaviour is consistent with a transition towards more ductile behaviour at higher confining pressures.

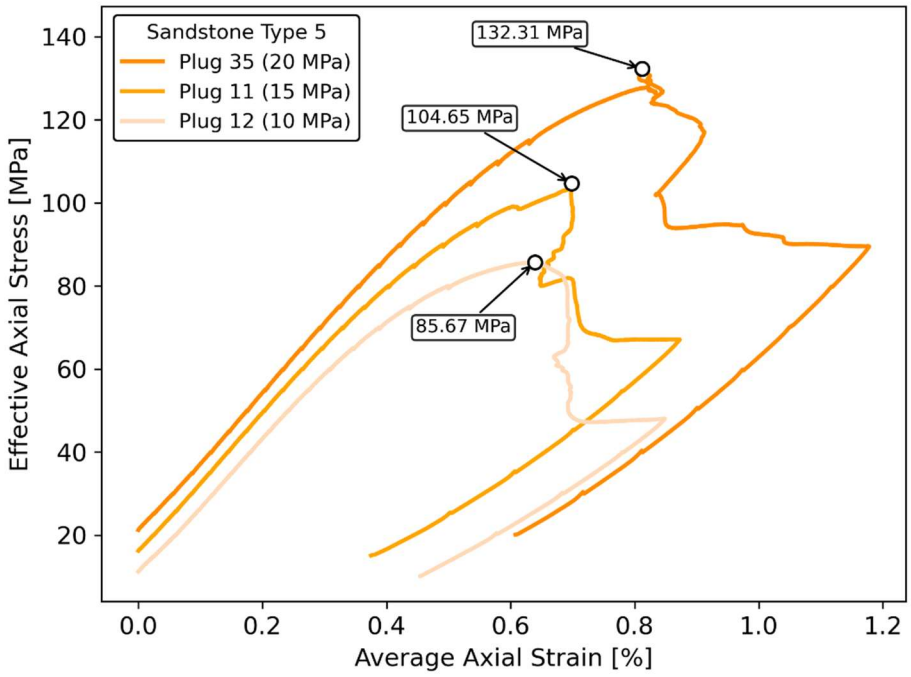


Figure 14. Effective axial stress and axial strain response of the three Sandstone Type 5 samples.

Static Young's modulus showed little variation across the three tests and ranged from 16.26 to 16.77 GPa. These values were generally higher than those obtained for Sandstone Types 1, 2, and 4. Poisson's ratio ranged from 0.102 to 0.162 and showed no systematic change with effective confining pressure (Table 3).

The failure behaviour of Sandstone Type 5 was characterised from the peak strength results using the Mohr-Coulomb failure criterion. Peak effective axial stress increased approximately linearly with effective confining pressure (Figure 15).

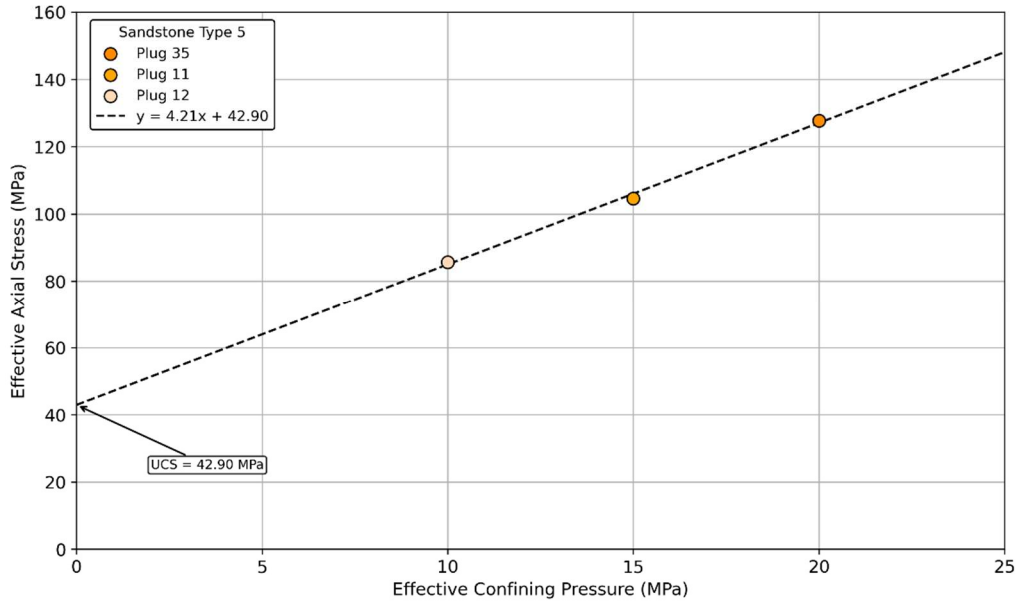


Figure 15. Relationship between peak effective axial stress and effective confining pressure for Sandstone Type 5. The dashed line shows the linear fit to the three test results, with extrapolation to zero effective confining pressure used to estimate UCS.

Extrapolation of the linear relationship to zero effective confining pressure gave an estimated UCS of 42.90 MPa, similar to the values obtained for Sandstone Types 2 and 4. In contrast, the friction angle of 38.02° was higher than both Sandstone Type 2 (29.21°) and Sandstone Type 4 (20.37°), reflecting the greater increase in peak strength with effective confining pressure. The resulting cohesion was 10.45 MPa (Figure 16; Table 4).

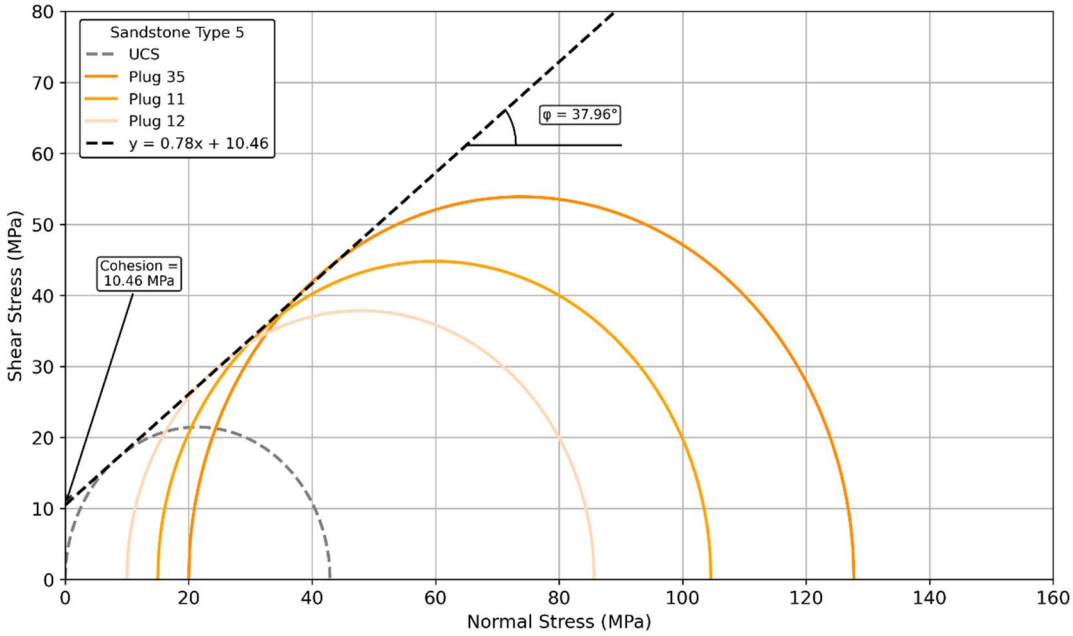


Figure 16. Mohr-Coulomb failure analysis for Sandstone Type 5. Mohr circles are shown for the three drained triaxial tests, together with the fitted failure envelope and extrapolated UCS circle.

5.1.6 Comparison of Mechanical Behaviour

Peak strength increased with effective confining pressure for all sandstone types, although the magnitude of this increase differed between groups. Sandstone Types 1 and 5 generally showed the highest peak strengths over the tested effective confining pressure range, while Sandstone Type 4 showed the lowest. Sandstone Type 3 showed greater variability, likely due to the peak strength outlier measured for Plug 34 at 20 MPa effective confining pressure.

The estimated parameters from the Mohr-Coulomb failure analysis also differed between sandstone types (Table 4). Sandstone Type 1 had the highest estimated UCS of 60.27 MPa. Sandstone Types 2, 4, and 5 had similar estimated UCS values of 43.72, 43.46, and 42.90 MPa, respectively, while Sandstone Type 3 had the lowest estimated UCS of 21.41 MPa. The pressure dependence of strength also varied between sandstone types, as shown by the friction angles. Sandstone Type 3 had the highest friction angle of 42.14°, followed by Sandstone Type 5 at 38.02°, Sandstone Type 1 at 30.93°, Sandstone Type 2 at 29.21°, and Sandstone Type 4 at 20.37°. However, the Sandstone Type 3 results should be used with cation as they are based on only two tests.

Differences were also observed in static Young's modulus. Sandstone Type 5 showed consistently high values of 16.26–16.77 GPa, while Sandstone Type 3 ranged from 15.52 to 18.16 GPa. Lower values were generally obtained for Sandstone Types 2 (13.08–14.48 GPa) and 4 (12.65–13.72 GPa). Sandstone Type 1 showed the greatest variation, ranging from 10.55 to 16.24 GPa, with the static Young's modulus increasing across the tested effective confining pressures. Overall, Young's modulus did not show a clear relationship with either peak strength or estimated UCS across the sandstone types. Static Poisson's ratio showed relatively narrow ranges for Sandstone Types 1, 2, and 5, with values of 0.143–0.179, 0.148–0.197, and 0.102–0.162, respectively. Greater variability was observed for Sandstone Types 3 and 4, including the unusually low values obtained for Plug 34 (0.0012) and Plug 31 (0.018) and the high value estimated for Plug 32 (0.414). No clear relationship was observed between static Poisson's ratio and effective confining pressure, static Young's modulus, or peak strength across the five sandstone types.

5.2 ACOUSTIC VELOCITY & DYNAMIC ELASTIC RESULTS

Acoustic velocities and isotropic-equivalent dynamic elastic properties were estimated for one representative plug from each sandstone type. The selected samples were Plugs 22, 25, 33, 31 and 35, representing Sandstone Types 1-5, respectively. Their effective confining pressures were 19, 18, 15, 18 and 20 MPa. Tables 5 and 6 summarises the measured P-wave and orthogonally polarised S-wave velocity ranges as well as the resultant calculated dynamic elastic properties. The individual measurements from each velocity stage are provided in Appendix 3 (Tables A3 and A4).

5.2.1 Acoustic Velocity Results

P-wave velocities ranged from 3219 to 3867 m/s across the five selected plugs, with Sandstone Type 5 (Plug 35) generally exhibiting the highest values. Plug 22 showed a modest overall increase in P-wave velocity during loading, while the remaining samples exhibited relatively stable or irregular responses. The two shear-wave channels generally showed greater variability, with S1 and S2 velocities ranging from 971 to 2113 m/s and 990 to 2012 m/s, respectively. Some samples exhibited overall increases in shear-wave velocity, while others showed substantial fluctuations between successive loading stages. Particularly large changes were observed for Plugs 25 and 33, preventing the identification of consistent stress-dependent relationships.

With increasing differential stress, acoustic velocities in sandstone are generally expected to increase as sample stiffness increases, followed by a reduction in the rate of increase as microcracking develops and an eventual decrease as cracking progresses towards failure. As the samples were already at their target effective confining pressures, much of the initial crack closure would have occurred before differential loading. However, the measured velocities did not consistently follow this expected trend, particularly the shear-wave measurements, which exhibited substantial fluctuations between successive loading stages.

Table 5. Summary of measured P-wave and orthogonally polarised S-wave velocities for the five sandstone types. Values represent the minimum and maximum recorded during differential loading.

Sandstone Type	Plug	V_p (m/s)	V_{S1} (m/s)	V_{S2} (m/s)
1	22	3291–3645	1912–2113	1739–2012
2	25	3219–3557	1015–1959	1032–1829
3	33	3316–3615	971–1885	990–1912
4	31	3232–3527	1792–1912	1506–1912
5	35	3402–3867	1750–2019	1709–1992

Although P- and S-wave velocities may respond differently to changes in sample stiffness and crack development, the magnitude and irregularity of some fluctuations also suggest possible uncertainty in waveform arrival identification. Variations in waveform quality may make it difficult to identify the same arrival consistently at successive loading stages, particularly for shear waves. The extent to which these variations reflect actual material behaviour or measurement uncertainty cannot be determined without further examination.

Acoustic measurements were generally recorded up to or near peak failure, with some tests capturing velocities close to the onset of failure. However, no consistent decrease in velocity was observed as failure approached. The irregularity of several measurements also made it difficult to identify changes associated with progressive cracking and damage.

Differences were observed between the two orthogonally polarised shear-wave velocities, with the higher velocity not consistently associated with the same measurement orientation. Although these differences may reflect directional variations in stiffness, the irregular fluctuations and changes in the relative velocities, particularly for Plugs 25 and 33, make it difficult to distinguish material behaviour from potential uncertainty in shear-wave arrival identification.

5.2.2 Dynamic Elastic Properties

The calculated isotropic-equivalent dynamic elastic properties varied between the five sandstone types and during loading. Dynamic Young's modulus ranged from 6.14 to 24.78 GPa, dynamic shear modulus from 2.10 to 9.94 GPa, dynamic bulk modulus from 11.55 to 25.84 GPa, and dynamic Poisson's ratio from 0.173 to 0.460 (Table 6). Plugs 22, 31, and 35 exhibited relatively narrow ranges of dynamic Young's modulus, whereas Plugs 25 and 33 showed substantially greater variation.

Table 6. Summary of calculated isotropic-equivalent dynamic elastic properties for the five sandstone types. Values represent the minimum and maximum calculated during differential loading using P-wave velocity, S1 velocity, and bulk density.

Sandstone Type	Plug	E_{dyn} (GPa)	v_{dyn} (-/-)	K_{dyn} (GPa)	G_{dyn} (GPa)
1	22	20.93–24.78	0.173–0.295	11.55–17.82	8.14–9.94
2	25	6.39–21.08	0.282–0.447	16.03–21.13	2.21–8.22
3	33	6.14–20.36	0.276–0.460	14.40–25.84	2.10–7.91
4	31	18.19–20.05	0.255–0.320	12.93–17.59	7.01–7.98
5	35	18.59–23.21	0.271–0.358	16.41–23.54	6.85–9.13

The dynamic properties were calculated using the measured P-wave velocity, the original S1-channel velocity, and the sample bulk density. S1 channel velocity was used consistently throughout the calculations to avoid changing the shear-wave input according to which channel recorded the higher velocity at a particular loading stage. This approach provides internally consistent estimates but does not fully characterise the anisotropic elastic response. Since the calculated Young's and shear moduli are particularly sensitive to the shear-wave velocity,

uncertainty in S1 arrival identification may contribute substantially to the wider ranges obtained for Plugs 25 and 33.

Dynamic Young's modulus is generally expected to be greater than the static Young's modulus. However, the particularly low S1 velocities recorded at certain loading stages for Plugs 25 and 33 directly resulted in calculated dynamic Young's moduli below the corresponding static values. Together with the substantial fluctuations in shear-wave velocity between successive loading stages, this raises concerns regarding the reliability of some shear-wave arrival identifications. Further examination of the recorded waveforms would help determine whether these measurements reflect true material behaviour or uncertainty in arrival picking.

Although the variability in the acoustic measurements limits the development of reliable stress-dependent velocity and dynamic stiffness relationships, the results provide property estimates that may help inform subsequent sandstone characterisation and modelling.

6 Concluding Remarks

This study was undertaken to characterise the geomechanical and acoustic properties of Gassum Formation sandstone from the Stenlille site, Denmark. Fifteen sandstone plugs representing five sandstone types were tested under drained triaxial conditions over a range of effective confining pressures. The programme provided measurements of peak strength and static elastic properties and allowed Mohr-Coulomb failure parameters to be determined for each sandstone type. Acoustic measurements were also collected during testing to characterise changes in P- and S-wave velocities and derive corresponding dynamic elastic properties.

Peak strength increased with effective confining pressure for all five sandstone types, although the strength and pressure-dependent response varied between groups. Sandstone Type 1 had the highest estimated UCS, while Sandstone Types 2, 4, and 5 had similar estimated UCS values but different friction angles. Static Young’s modulus also varied between sandstone types but showed no clear relationship with either peak strength or estimated UCS. As effective confining pressure increased, the samples generally showed a smaller stress drop following sample failure and a more gradual transition towards the residual stress state. This behaviour is consistent with the typical response of rock as deformation becomes less brittle with increasing confining pressure and approaches the brittle–ductile transition. The Sandstone Type 3 results showed greater variability and did not define a consistent three-point strength relationship. Its reported Mohr-Coulomb parameters are therefore based on two failure points and should be treated with caution.

The acoustic measurements provided additional characterisation of the dynamic elastic response of the five sandstone types. Differences in velocity and calculated dynamic stiffness were observed between samples, with some exhibiting modest overall increases during loading. However, substantial fluctuations in several shear-wave measurements limited the identification of consistent stress-dependent relationships and potential velocity reductions preceding failure. The particularly low S1 velocities recorded for Plugs 25 and 33 produced calculated dynamic Young's moduli below the corresponding static values at certain loading stages. Combined with the irregular shear-wave responses, these results indicate that some waveform arrival identifications warrant further examination to distinguish measurement uncertainty from changes in material behaviour. Although the variability limits the use of these measurements to establish reliable stress-dependent relationships, the measured velocities and calculated dynamic properties provide useful ranges for subsequent sandstone characterisation and modelling. Comparison with available borehole sonic log-derived velocities would help assess the representativeness of these ranges under in-situ conditions.

Overall, the laboratory programme provides a consistent set of strength, static elastic, and acoustic properties for the tested Gassum Formation sandstone and characterises their response to changing effective stress conditions. These results provide geomechanical parameters for the Stenlille sandstone intervals and a basis for their application within the wider project objectives described in Section 1.

Appendix 1 Synthetic Brine Composition

A synthetic brine representative of Gassum Formation water at Stenlille was used as the pore fluid during sample saturation and drained triaxial testing. The brine recipe was based on Gassum Formation water from the Stenlille-18 well at 1662 m depth, using formation water data from AQUA-DK. The chemical composition was subsequently modified using data from Stenlille-1. The quantities of individual compounds used to prepare the synthetic solution are given in Table A1, with the calculated bulk properties of the resulting brine summarised in Table A2.

Table A 1. Composition of the synthetic brine used for sample saturation and drained triaxial testing.

Element	Element concentration (mg/L)	Compound	Compound concentration (g/L)	Concentration (mol/L)
Na^+	59135	NaCl	150.327	2.5722
Na^+	11	$NaHCO_3$	0.041	0.0005
Na^+	248	NaBr	1.111	0.0108
K^+	308	KCl	0.587	0.0079
Mg^{2+}	1803	$MgCl_2 \cdot 6H_2O$	15.082	0.0742
Mg^{2+}	35	$MgSO_4 \cdot 7H_2O$	0.354	0.0014
Ca^{2+}	9964	$CaCl_2 \cdot 2H_2O$	36.550	0.2486

Table A 2. Calculated bulk properties of the synthetic brine.

Property	Value	Unit
Total dissolved solids (TDS)	186032.47	mg/L
Estimated density at 20C	1.118	g/mL
Salinity	16.627	Wt%
NaCl equivalent concentration	3.18	mol/L

Appendix 2 Estimation of Overburden Stress

Vertical stress profiles were estimated for the Stenlille wells to provide representative in-situ stress conditions for the selection of the confining pressures used during drained triaxial testing. Calculation of vertical stress requires a bulk density profile with depth from the surface to the target sample intervals. As direct density measurements were not available over the full depth range, a representative density profile was constructed using the available well log data together with estimated densities where required.

Previous studies indicate that the Stenlille area has undergone approximately 600 m of exhumation (Japsen & Bidstrup, 1999; Japsen et al., 2007). Based on the regional well compilation of Fabricius (2007), a chalk porosity of approximately 50% was considered representative at 600 m depth below the surface. Using a formation fluid density of 1.08 g/cm³ for Stenlille (Pasquinelli et al., 2020) and a calcite mineral density of 2.71 g/cm³ (Mavko et al., 2020), this corresponds to an estimated chalk bulk density of approximately 1.89 g/cm³.

Vertical stress profiles were calculated for the Stenlille-6 and Stenlille-10 wells. Where available, measured bulk density (RHOB) logs were used to constrain the density profile. Density was also estimated from sonic slowness using a Gardner transform, with a factor of 1.84923 and exponent of 0.0306366. These data were combined with extrapolated densities based on the estimated near-surface density and the measured or sonic-derived densities at depth to construct a continuous composite density profile for each well.

The composite density profiles were integrated with depth to estimate the vertical stress. The resulting depth-vertical stress relationships were subsequently used to estimate the vertical stress at the depth of each test sample and to guide selection of the confining pressures used in the laboratory programme. The well log data and density profiles used in the calculations for Stenlille-6 and Stenlille-10 are shown separately in Figures A1 and A2, respectively.

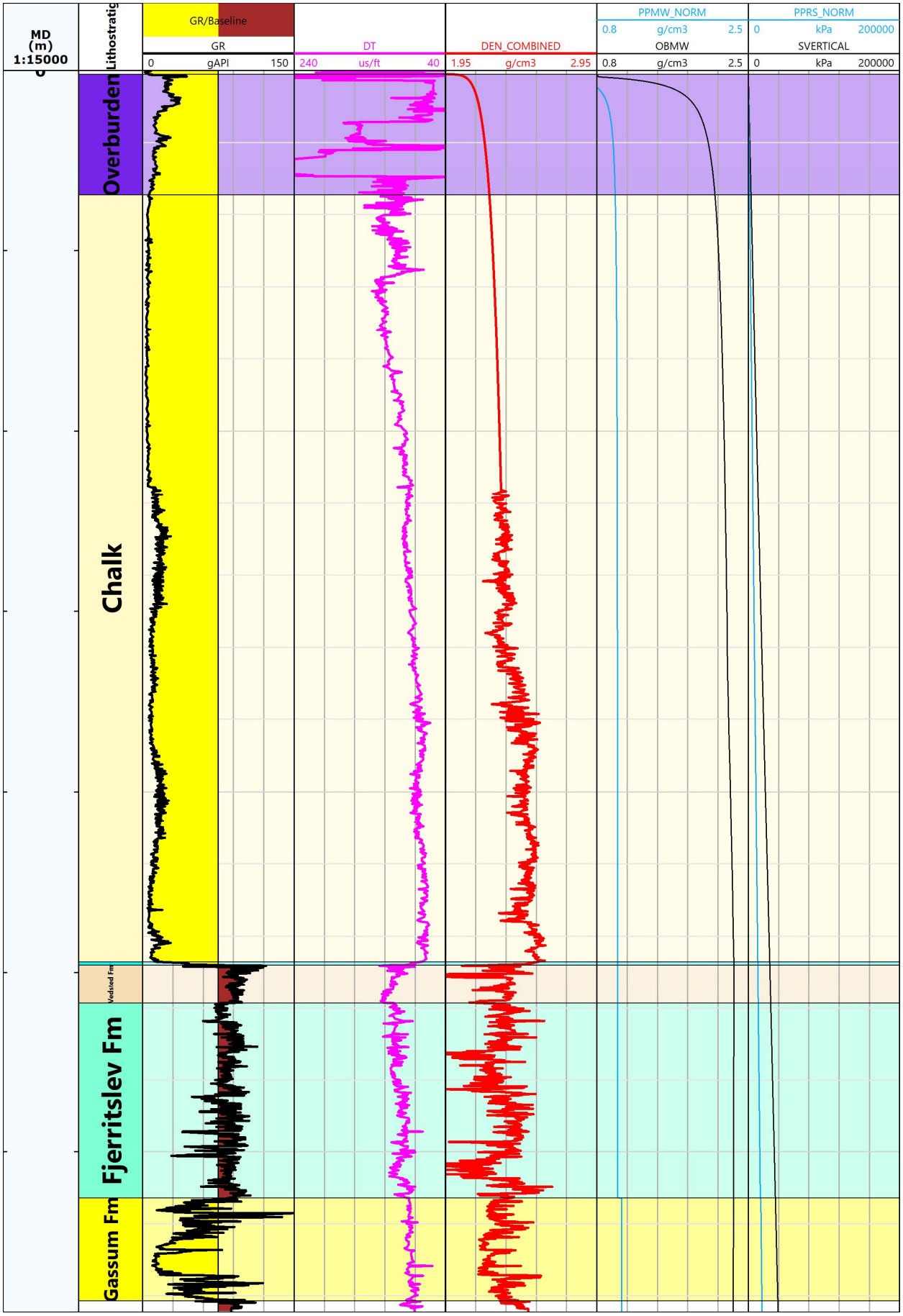


Figure A 1. Well log data and composite density profile used to estimate vertical stress for the Stenlille-6 well. Available bulk-density and sonic-log data provided by GEUS/Gas Storage Denmark were combined with estimated densities to construct the density profile used for integration with depth.

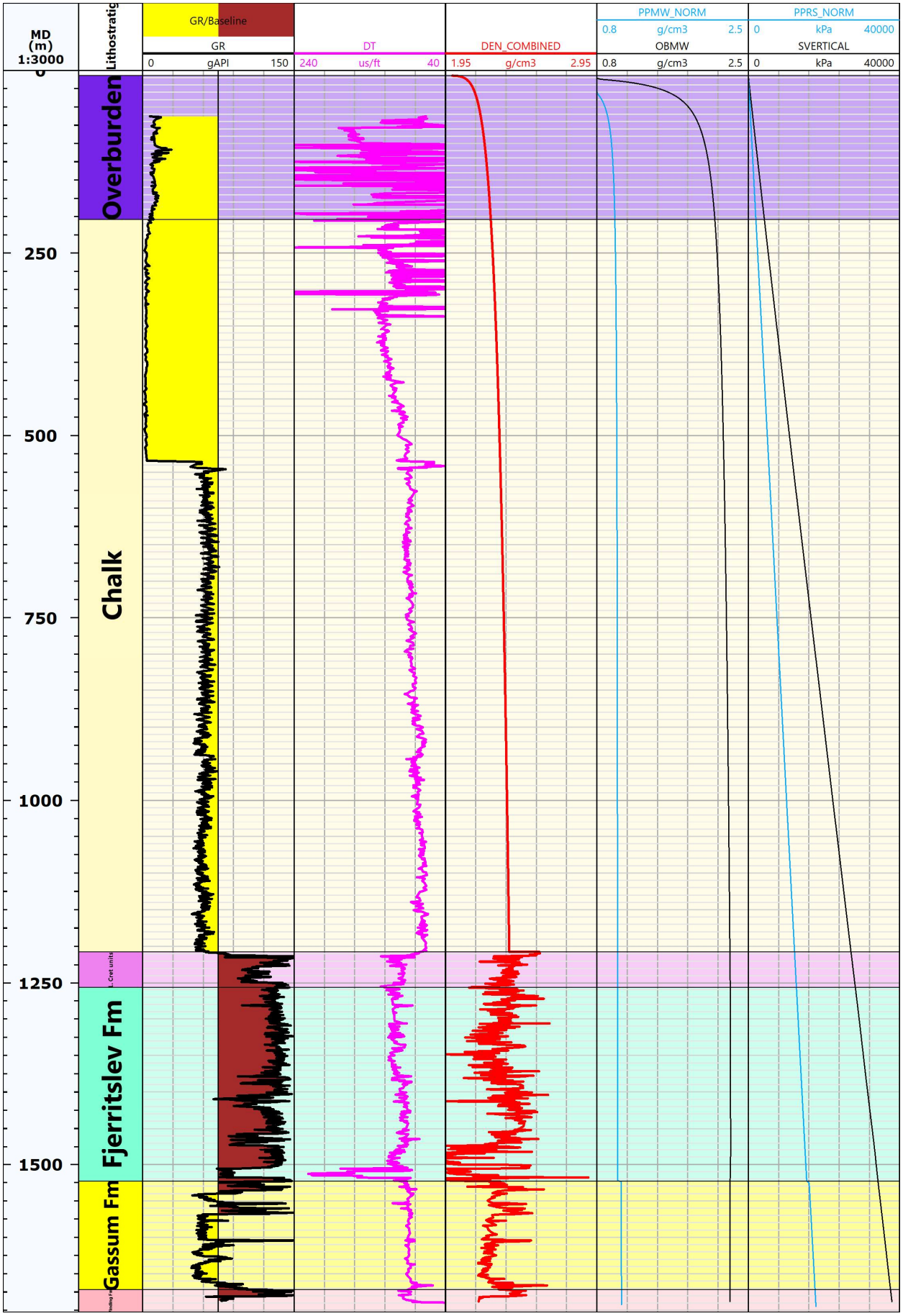


Figure A 2. Well log data and composite density profile used to estimate vertical stress for the Stenlille-10 well. Available bulk-density and sonic-log data provided by GEUS/Gas Storage Denmark were combined with estimated densities to construct the density profile used for integration with depth.

Appendix 3 Acoustic Velocity & Dynamic Elastic Data

This appendix presents the complete acoustic velocity measurements and calculated isotropic-equivalent dynamic elastic properties for the five selected sandstone plugs. Table A3 provides the P-wave and orthogonally polarised S-wave velocities measured at each differential stress step, while Table A4 presents the corresponding dynamic Young's modulus, Poisson's ratio, bulk modulus, shear modulus, and shear-wave velocity contrast.

The S1 and S2 measurements represent two fixed orthogonal shear-wave polarisations rather than consistently faster and slower shear-wave velocities. Their percentage velocity contrast was calculated as:

$$C = \frac{|V_{S1} - V_{S2}|}{\max(V_{S1}, V_{S2})} \times 100 \quad \text{(A1)}$$

where (C) is the shear-wave velocity contrast (%). The calculation uses the absolute velocity difference normalised by the higher measured velocity at each loading stage.

The calculated contrast provides a measure of the difference between the two shear-wave measurements. However, given the variability observed during loading, particularly for Plugs 25 and 33, these values should not be interpreted as definitive estimates of elastic anisotropy or its evolution with differential stress.

Table A 3. P-wave and orthogonally polarised S-wave velocities measured at individual differential stress stages for the five selected sandstone plugs.

Sandstone Type	Plug	Differential stress (MPa)	V_p (m/s)	V_{S1} (m/s)	V_{S2} (m/s)
1	22	5	3291	2057	1746
1	22	10	3316	2085	1759
1	22	15	3473	1916	1786
1	22	20	3500	1986	1739
1	22	25	3500	1912	1807
1	22	30	3500	1928	1786
1	22	35	3500	1965	1759
1	22	40	3615	1948	1807
1	22	50	3529	1920	1800
1	22	60	3557	1924	2003
1	22	70	3645	2113	1969
1	22	80	3529	2071	1995
1	22	90	3615	2030	2012
1	22	100	3500	2016	1858
2	25	1	3267	1015	1032
2	25	5	3219	1266	1130
2	25	10	3529	1392	1373
2	25	15	3341	1391	1473
2	25	20	3478	1380	1483
2	25	25	3393	1496	1406
2	25	30	3393	1497	1584
2	25	35	3291	1584	1693
2	25	40	3341	1652	1558
2	25	50	3291	1539	1579
2	25	60	3557	1959	1829

Sandstone Type	Plug	Differential stress (MPa)	V_p (m/s)	V_{S1} (m/s)	V_{S2} (m/s)
2	25	68	3367	1537	1753
2	25	75	3243	1464	1746
2	25	77	3291	1497	1517
3	33	1	3586	971	990
3	33	10	3446	1885	1568
3	33	15	3370	1385	1381
3	33	20	3505	1670	1274
3	33	25	3498	1720	1292
3	33	30	3393	1714	1759
3	33	35	3316	1844	1822
3	33	40	3341	1833	1720
3	33	50	3419	1800	1746
3	33	60	3557	1692	1912
3	33	70	3446	1692	1881
3	33	75	3615	1723	1646
3	33	80	3393	1825	1793
4	31	1	3337	1792	1564
4	31	5	3333	1806	1512
4	31	10	3232	1842	1506
4	31	15	3527	1813	1873
4	31	20	3337	1813	1778
4	31	25	3337	1904	1858
4	31	30	3337	1850	1785
4	31	35	3339	1817	1785
4	31	40	3333	1881	1912
4	31	50	3337	1912	1881
5	35	1	3402	1785	1844
5	35	5	3458	1851	1750
5	35	10	3515	1844	1915
5	35	15	3667	1792	1844
5	35	20	3698	1750	1821
5	35	25	3544	1844	1836
5	35	30	3867	1825	1736
5	35	35	3604	1760	1821
5	35	40	3867	1859	1799
5	35	50	3604	1788	1867
5	35	60	3798	1788	1736
5	35	70	3604	1895	1836
5	35	80	3832	1875	1709
5	35	90	3832	1944	1709
5	35	102	3604	2019	1992

Table A 4. Calculated dynamic elastic properties and shear-wave velocity contrast at individual differential stress stages for the five selected sandstone plugs.

Sandstone Type	Plug	Differential stress (MPa)	E_{dyn} (GPa)	v_{dyn} (-/-)	K_{dyn} (GPa)	G_{dyn} (GPa)	S-wave contrast (%)
1	22	5	22.21	0.180	11.55	9.41	15.1
1	22	10	22.69	0.173	11.57	9.67	15.6
1	22	15	20.93	0.281	15.94	8.17	6.8
1	22	20	22.16	0.263	15.56	8.78	12.4
1	22	25	20.95	0.287	16.42	8.14	5.5
1	22	30	21.21	0.282	16.23	8.27	7.3
1	22	35	21.82	0.270	15.81	8.59	10.5
1	22	40	21.88	0.295	17.82	8.45	7.2
1	22	50	21.16	0.290	16.77	8.20	6.2
1	22	60	21.31	0.293	17.17	8.24	4.0
1	22	70	24.78	0.247	16.32	9.94	6.8
1	22	80	23.61	0.237	14.98	9.54	3.7
1	22	90	23.28	0.270	16.86	9.17	0.9
1	22	100	22.65	0.252	15.20	9.05	7.8
2	25	1	6.39	0.447	19.92	2.21	1.6
2	25	5	9.66	0.409	17.62	3.43	10.7
2	25	10	11.68	0.408	21.13	4.15	1.4
2	25	15	11.56	0.395	18.39	4.14	5.6
2	25	20	11.48	0.407	20.47	4.08	6.9
2	25	25	13.22	0.379	18.26	4.79	6.0
2	25	30	13.24	0.379	18.25	4.80	5.5
2	25	35	14.51	0.349	16.03	5.38	6.4
2	25	40	15.65	0.338	16.11	5.85	5.7
2	25	50	13.81	0.360	16.43	5.08	2.5
2	25	60	21.08	0.282	16.13	8.22	6.7
2	25	68	13.84	0.368	17.53	5.06	12.3
2	25	75	12.59	0.372	16.40	4.59	16.2
2	25	77	13.15	0.370	16.80	4.80	1.3
3	33	1	6.14	0.460	25.84	2.10	1.9
3	33	10	20.36	0.286	15.90	7.91	16.8
3	33	15	11.95	0.398	19.61	4.27	0.3
3	33	20	16.82	0.353	19.08	6.21	23.7
3	33	25	17.67	0.341	18.47	6.59	24.9
3	33	30	17.38	0.329	16.92	6.54	2.6
3	33	35	19.33	0.276	14.40	7.57	1.2
3	33	40	19.22	0.285	14.90	7.48	6.1
3	33	50	18.89	0.308	16.41	7.22	3.0
3	33	60	17.26	0.354	19.69	6.37	11.5
3	33	70	17.10	0.341	17.95	6.37	10.1
3	33	75	17.90	0.353	20.30	6.61	4.5
3	33	80	19.24	0.296	15.74	7.42	1.7
4	31	1	18.19	0.297	14.96	7.01	12.7
4	31	5	18.40	0.292	14.76	7.12	16.3
4	31	10	18.67	0.259	12.93	7.41	18.2
4	31	15	18.95	0.320	17.59	7.18	3.2

Sandstone Type	Plug	Differential stress (MPa)	E_{dyn} (GPa)	v_{dyn} (-/-)	K_{dyn} (GPa)	G_{dyn} (GPa)	S-wave contrast (%)
4	31	20	18.52	0.291	14.74	7.18	2.0
4	31	25	19.93	0.259	13.75	7.92	2.5
4	31	30	19.10	0.278	14.35	7.47	3.5
4	31	35	18.59	0.290	14.74	7.21	1.8
4	31	40	19.56	0.266	13.96	7.72	1.7
4	31	50	20.05	0.255	13.66	7.98	1.7
5	35	1	18.69	0.310	16.41	7.13	3.2
5	35	5	19.94	0.299	16.53	7.67	5.5
5	35	10	19.94	0.310	17.51	7.61	3.7
5	35	15	19.31	0.343	20.52	7.19	2.8
5	35	20	18.59	0.356	21.49	6.85	3.9
5	35	25	20.01	0.314	17.98	7.61	0.4
5	35	30	20.23	0.357	23.54	7.46	4.9
5	35	35	18.64	0.343	19.84	6.94	3.4
5	35	40	20.89	0.350	23.16	7.74	3.2
5	35	50	19.14	0.337	19.54	7.16	4.2
5	35	60	19.44	0.358	22.75	7.16	2.9
5	35	70	21.04	0.309	18.37	8.04	3.1
5	35	80	21.13	0.343	22.38	7.87	8.8
5	35	90	22.46	0.327	21.59	8.46	12.1
5	35	102	23.21	0.271	16.91	9.13	1.3

Glossary

BGS British Geological Survey

GEUS Geological Survey of Denmark and Greenland

ISRM International Society for Rock Mechanics and Rock Engineering

MD Measured depth. Depth measured along the path of a wellbore

UCS Unconfined compressive strength

Young's Modulus Measure of a material's stiffness

Poisson's Ratio Ratio of lateral strain to axial strain during loading

Bulk Modulus Measure of resistance to shear deformation

Shear Modulus Measure of resistance to shear deformation

Static elastic properties Elastic properties determined from loading (i.e., stress-strain)

Dynamic elastic properties Elastic properties calculated from acoustic wave velocities

P-wave Compressional wave in which motion is parallel to the direction of wave propagation

S-wave Shear wave in which motion is perpendicular to the direction of wave propagation

S1 / S2 Fast and slow orthogonally polarised shear waves

Shear-wave splitting Difference between the fast and slow S-waves

PZT Piezoelectric transducer. A device used to generate and/or detect acoustic waves

PTFE Polytetrafluoroethylene. Polymer material used to jacket the test samples

TDS Total dissolved solids. The total concentration of dissolved substances in a fluid

RHOB Bulk density well log used to determine formation density with depth

References

Andrianov, N. et al, 2024. Results of risk and safety assessment and description of monitoring program. ConsenCUS deliverable D4.5, https://consencus.eu/results.

Bredesen, K. 2022. Assessing rock physics and seismic characteristics of the Gassum Formation in the Stenlille aquifer gas storage – A reservoir analog for the Havnsø CO2 storage prospect, Denmark. International Journal of Greenhouse Gas Control. https://doi.org/10.1016/j.ijggc.2022.103583.

Fabricius, I.L., 2007. Chalk: composition, diagenesis and physical properties. Bulletin of the Geological Society of Denmark, 55, pp.97–128.

Holmslykke, H. D., Olivarius, M., Kjøller, C., & Dideriksen, K. 2020. Capture, Storage and Use of CO2 (CCUS). Reservoir characterisation and hydrogeochemical reactions between CO2 and reservoir rock. GEUS. Danmarks og Grønlands Geologiske Undersøgelse Rapport Vol. 2020 No. 29 https://doi.org/10.22008/gpub/34526.

Japsen, P. and Bidstrup, T., 1999. Quantification of late Cenozoic erosion in Denmark based on sonic data and basin modelling. Bulletin of the Geological Society of Denmark, 46, pp.79–99.

Japsen, P., Green, P.F., Nielsen, L.H., Rasmussen, E.S. and Bidstrup, T., 2007. Mesozoic–Cenozoic exhumation events in the eastern North Sea Basin: a multi-disciplinary approach based on palaeothermal, palaeoburial, stratigraphic and seismic data. Basin Research, 19, pp.451–490.

ISRM, 2007. The complete ISRM suggested methods for rock characterization, testing and monitoring: 1974–2006. In: Ulusay R, Hudson JA (eds) Suggested methods. prepared by ISRM commission on testing methods. Compilation Arranged by ISRM Turkish National Group, Ankara.

Kristensen, L. 2021. Capture, Storage and Use of CO2 (CCUS). Reservoir data - Stenlille area (Part of Work package 6). GEUS. Danmarks og Grønlands Geologiske Undersøgelse Rapport Vol. 2020 No. 28 https://doi.org/10.22008/gpub/34525.

Mavko, G., Mukerji, T. and Dvorkin, J., 2020. The rock physics handbook. 3rd ed. Cambridge: Cambridge University Press.

Naderloo, M., Kumar, K.R., Hernandez, E., Hajibeygi, H. and Barnhoorn, A., 2023. Experimental and numerical investigation of sandstone deformation under cycling loading relevant for underground energy storage. Journal of Energy Storage, 64, p.107198.

Nicksiar, M. and Martin, C.D., 2012. Evaluation of methods for determining crack initiation in compression tests on low-porosity rocks. Rock mechanics and rock engineering, 45(4), pp.607-617.

Pasquinelli, L., Felder, M., Gulbrandsen, M.L., Hansen, T.M., Jeon, J.S., Molenaar, N., Mosegaard, K. and Fabricius, I.L., 2020. The feasibility of high-temperature aquifer thermal energy storage in Denmark: The Gassum Formation in the Stenlille structure. Bulletin of the Geological Society of Denmark, 68, pp.133–154.